Missouri S&T Library and Learning Resources

Scholars' Mine

Doctoral Dissertations

Student Theses and Dissertations

Summer 2017

Control of single- and dual-probe atomic force microscopy

Muthukumaran Loganathan

Follow this and additional works at: https://scholarsmine.mst.edu/doctoral_dissertations

Part of the Electrical and Computer Engineering Commons, and the Mechanical Engineering Commons

Department: Mechanical and Aerospace Engineering

Recommended Citation

Loganathan, Muthukumaran, "Control of single- and dual-probe atomic force microscopy" (2017). *Doctoral Dissertations*. 2995.
https://scholarsmine.mst.edu/doctoral_dissertations/2995

This thesis is brought to you by Scholars' Mine, a service of the Missouri S&T Library and Learning Resources. This work is protected by U. S. Copyright Law. Unauthorized use including reproduction for redistribution requires the permission of the copyright holder. For more information, please contact scholarsmine@mst.edu.

CONTROL OF SINGLE- AND DUAL-PROBE ATOMIC FORCE MICROSCOPY

by

MUTHUKUMARAN LOGANATHAN

A DISSERTATION

Presented to the Faculty of the Graduate School of the

MISSOURI UNIVERSITY OF SCIENCE AND TECHNOLOGY

In Partial Fulfillment of the Requirements for the Degree

DOCTOR OF PHILOSOPHY
in
MECHANICAL ENGINEERING

2017

Approved
Douglas A. Bristow, Advisor
Robert G. Landers
Jagannathan Sarangapani
Edward C. Kinzel
Richard K. Brow

PUBLICATION DISSERTATION OPTION

This thesis consists of two articles which have been submitted for publication, or will be submitted for publication as follows:

PAPER I: Pages 10-34 are intended for submission to IEEE Transactions on Control Systems Technology.

PAPER II: Pages 35-70 have been submitted to IEEE Transactions on Mechatronics.

ABSTRACT

Atomic force microscope (AFM) is one of the important and versatile tools available in the field of nanotechnology. It is a type of probe-based microscopy wherein an atomically sharp tip, mounted on the free end of a microcantilever, probes the surface of interest to generate 3D topographical images with nanoscale resolution. An integral part of the AFM is the feedback controller that regulates the probe deflection in the presence of surface height changes, enabling the control action to be used for generating topographical image of the sample. Besides sensing, the probe can also be used as a mechanical actuator to manipulate nanoparticles and fabricate nanoscale structures. Despite its capabilities, AFM is not considered user-friendly because imaging is slow, and fabrication operations are laborious and often performed in open-loop, i.e. without any monitoring mechanism. This dissertation is composed of two journal articles which aim to address prominent AFM challenges using feedback control strategies. First article proposes a novel control design methodology based on repetitive control technique to accurately track AFM samples. Theoretical and experimental results demonstrate that incorporating a model of the general sample topography in the control design leads to superior tracking in AFM. Second article introduces a novel dual-probe AFM (DP-AFM) design that has two independent probes. Such a setup provides an opportunity to implement process control strategies where one probe can be used to perform one of the many AFM operations while the other probe can provide feedback by imaging the process. To demonstrate this capability, an application involving real-time plowing depth control where plow depth is controlled with nanometer-level accuracy is also presented.

ACKNOWLEDGMENTS

I would like to thank my advisor, Dr. Douglas Bristow, for his impeccable mentorship, guidance, and infinite patience which made this work possible. His willingness to believe in me, more than I believed in myself, made me realize my true potential. The years I spent in Missouri S&T working under him have transformed me not only into an engineering professional, but into a better person as well.

I would like to acknowledge the financial support from the National Science Foundation (CMMI-1229701) and the Intelligent Systems Center (ISC) at Missouri S&T. I thank the Material Research Center (MRC) for providing uninterrupted access to their equipment, and Dr. Eric Bohannan for his help with the AFM. I would like to thank Dr. Robert Landers, Dr. Jagannathan Sarangapani, Dr. Edward Kinzel and Dr. Richard Brow for graciously accepting to be on my dissertation committee. A special thank you to my colleagues in the Precision Motion Control Lab, particularly Ayad and Mohsen for sharing their knowledge and expertise on AFM.

There are no words to express my gratitude to my family and friends who have been very supportive of me during my time in graduate school, especially to my mother who has been nothing short of amazing. Lastly, I thank the United States of America and its people for welcoming me into this country and being a great host for these past seven years.

TABLE OF CONTENTS

Page

PUBLICATION DISSERTATION OPTION...iii

ABSTRACT...iv

ACKNOWLEDGMENTS v

LIST OF ILLUSTRATIONS...viii

LIST OF TABLES...xi

SECTION

1. INTRODUCTION...1

1.1. ATOMIC FORCE MICROSCOPY..1

1.1.1. Feedback Control in AFM...3

1.1.2. Nanofabrication Using AFM..5

1.1.3. Multi-Probe AFM Systems...7

1.2 REPETITIVE CONTROL...9

PAPER

I. A QUASI-REPETITIVE CONTROLLER FOR ACCURATE IMAGING IN ATOMIC FORCE MICROSCOPY..10

ABSTRACT...10

1. INTRODUCTION 11

2. QUASIPERIODIC SIGNAL MODELING..13

2.1. ADDITIVE QUASIPERIODIC SIGNALS 13

2.2. MULTIPLICATIVE QUASIPERIODIC SIGNALS 15

2.3. AFM SAMPLE MODELING 19

3. QUASI-REPETITIVE CONTROL DESIGN...22

3.1. CONTROLLER IMPLEMENTATION..23

4. EXPERIMENTAL RESULTS & DISCUSSION..26

5. CONCLUSIONS...31

REFERENCES...32

II. DESIGN AND CONTROL OF A DUAL-PROBE ATOMIC FORCE MICROSCOPE...35

ABSTRACT 35
1. INTRODUCTION 36
2. SYSTEM DESIGN 38
2.1. OPTICAL LEVER DESIGN 41
2.2. CONTROLLER AND SOFTWARE DESIGN 46
3. DP-AFM CALIBRATION PROCEDURES 49
3.1. 3D PROBE POSITION ERROR COMPENSATION 50
3.2. DUAL-PROBE ALIGNMENT PROCEDURE 54
4. CLOSED-LOOP PLOWING 57
4.1. PLOWING MODEL DESCRIPTION 58
4.2. CONTROL FORMULATION 60
5. EXPERIMENTAL RESULTS & DISCUSSION 64
6. CONCLUSIONS 67
REFERENCES 68
SECTION
2. CONCLUSIONS 71
APPENDICES
A. LABVIEW PROGRAMS FOR DP-AFM OPERATION 72
B. MATLAB PROGRAMS FOR AFM IMAGE PROCESSING 87
BIBLIOGRAPHY 91
VITA 96

LIST OF ILLUSTRATIONS

Figure Page

1.1. Schematic of an AFM. 2

1.2. SEM images of (a) Typical AFM microcantilever with a sharp tip at the end, (b) zoomed-in view of the AFM tip. 2

1.3. Illustration of a typical AFM control loop. 4

1.4. Illustration of (a) nanomanipulation using AFM probe, (b) dip-pen nanolithography process and (c) Nano plowing process. 6

1.5. Multi-probe AFM systems presented in the literature. (a) A dual-probe AFM with two optical lever for each probe [33], (b) dual-probe design with a self-sensing AFM probe [35] and (c) a quadruple-probe AFM. 8

PAPER I

1. Illustration of (a) Typical AFM sample topography, and (b) The time-history of the height signal when the sample is raster scanned. 11

2. An illustrative example of (a) a periodic signal, (b) a polynomial signal, (c) an additive quasiperiodic (AQP) signal composed of (a) and (b), (d) a multiplicative quasiperiodic (MQP) signal composed of (a) and (b). 13

3. Illustration of an AFM control loop for regulating tip deflection. The sample height acts as the disturbance on the control loop while the tip scans the sample. 20

4. Typical raster pattern involved in scanning an AFM sample in (a) spatial domain, and (b) the time domain signals corresponding to individual axes to generate the raster pattern. 21

5. A generalized repetitive controller frame work. The highlighted section of the controller, $S(z)$, represents the internal model of a periodic signal. 23

6. Multi-buffer internal model structure for a quasiperiodic signal. 25

7. Experimental results corresponding to imaging a Magnetite sample. (a) 3D image of the sample is inclined due to the misalignment between the sample and the raster plane, (b) Raster profile of the scanner, sample height, and the tracking error of PI and PI+QRC schemes corresponding to 6 raster cycles. 27

8. Magnetite sample imaged using a (a) PI controller and (b) PI+QRC controller. The tracking error of PI (PI_{RMS} = 12.3 nm) and PI +QRC (QRC_{RMS}= 3.9 nm) schemes are plotted in spatial domain in (c) and (d). 28

9. Image of a glass rod sample obtained using (a) PI controller and (b) PI+QRC combination. The tracking error of PI (PI_{RMS} = 28.1 nm) and PI +QRC (QRC_{RMS}= 5.2 nm) schemes are plotted in spatial domain in (c) and (d). Comparison of tracking error of PI and PI+QRC at the dotted line marked in (c) and (d) is shown in (e). 30

PAPER II

1. Illustration of (a) opposing dual probe configuration with top visual probes and (b) manipulation application using the two opposing probes...........................39

2. Schematic of dual probe arrangement (a), image of the actual DP-AFM setup (b), zoomed in image showing the probe holders with dither piezos (c), and the camera view (top view) of the two top visual probes aligned tip-to-tip (d). 40

3. Schematic of a typical optical lever setup (a), laser spot displacement on the PSD which comprises of four photodetector quadrants A-D (b), schematic illustrating the cone angle of the diverging laser beam directed towards the PSD (c)..42

4. Experimental PSD voltage vs. sample stage displacement (Approach-retract curve). The slope of the linear segment is 0.8 mV/nm, which is the experimental OLS..46

5. Instrument control layout showing the interconnections of various components of the DP-AFM. 47

6. Schematic of (a) software components involved in operating a single probe for imaging. The other probe involves identical components for its operation, and hence is not shown. Block diagram representation of a RMS filter is shown in (b). 49

7. Illustration of (a) laser spot displacement on the PSD due to tip deflection, and (b) spot displacement due to change in probe position which could be misinterpreted as tip deflection. 51

8. Plots showing (a) Quasi-random motion of the individual probe axes, and (b) Comparison between compensated and uncompensated deflection signal when the probe stages are traversed in a quasi-random trajectory. 53

9. Steps involved in aligning the probes in 3D space. (a) Probe 1 is engaged to the sample. (b) Probe 2 is engaged to the sample. (c) Sample is withdrawn leaving the probes approximately in the same XY plane. (d) 2D raster search pattern traversed by the moving probe. (e) Two probes in contact with each other. 55

10. The horizontal channel signal of a contact and tapping-mode probes when contact mode probe was used to raster search the tapping-mode probe. The inset shows the different stages of contact while searching for the probe. 56

11. Schematic of the plowing process (a), Spring-mass-damper representation of the probe-substrate interaction (b), and tip-to-tip probe setup in DP-AFM for plowing process control (c). The imaging probe trails the plowing probe by a spatial offset of Δx, which induces a time delay in the plow depth measured by the imaging probe..........59

12. Block diagram representation of the plowing process control. The continuous plowing process is measured at discrete time intervals of size T_{im} which correspond to the scan rate of the imaging probe. The scan line data arrives at rate of 1-10 Hz and is upscaled using zero-order hold method to match the controller execution rate of 100 Hz. 62

13. Plots showing (a) raw scan line data of the plow section generated by the imaging probe and the best line fit of the data, and (b) flattened scan line obtained by subtracting the best line fit from the raw data. 63

14. 2D images of two sets 4 parallel lines plowed in different locations on the same substrate. The section images show the variation in the plow depth due to the presence of process uncertainties. 64

15. 2D image of the plowed profile with a step change in depth of cut from 10 to 25 nm, and the plow depth with respect to the plow probe position are shown in (a). The scan line data of the plowed line at the location marked by the green arrows in Figure 15(a) is plotted in (b)..........66

LIST OF TABLES

Table Page

1. Gain Values For QRC up to Order 4 26

1. INTRODUCTION

The ability to visualize and manipulate matter at the nanoscale has always been of great interest to the scientific and engineering community. Such capabilities are enabled by precision systems like scanning electron microscope (SEM), scanning tunneling microscope (STM), scanning near-field optical microscope (SNOM), and atomic force microscope (AFM). However, the ever-increasing demand for precise, accurate, and complicated nanoscale operations warrants the need to push the boundaries of these systems. This dissertation focuses on atomic force microcopy and precision motion control techniques that improve and extend its capabilities.

1.1. ATOMIC FORCE MICROPSCOPY

The atomic force microscope (AFM) was invented by Binnig *et al.* [1] in 1986 to study non-conducting surfaces at the atomic level. The principle of operation is straight forward. A sharp, nano-sized tip, mounted on a microcantilever, is made to raster scan the sample of interest. Changes in the surface height induce a change in the probe deflection which is measured using an optical lever arrangement [2]. An optical lever involves measuring the probe deflection by focusing a laser beam on the top face of the inclined microcantilever and capturing the laser beam displacement using a position-sensitive photodetector (PSD). A feedback controller regulates the deflection to a constant set point by controlling the z-axis position of the 3-axis nanostage on which the sample is loaded. The resulting control action is used to generate a 3D digital image of the sample. Figure 1.1 shows the integral components of the AFM and Figure 1.2 shows a typical

AFM microcantilever with a sharp tip on its end. The AFM tips are often etched out of silicon, however probes made of different materials like diamond and carbon nanotubes are also available for special applications.

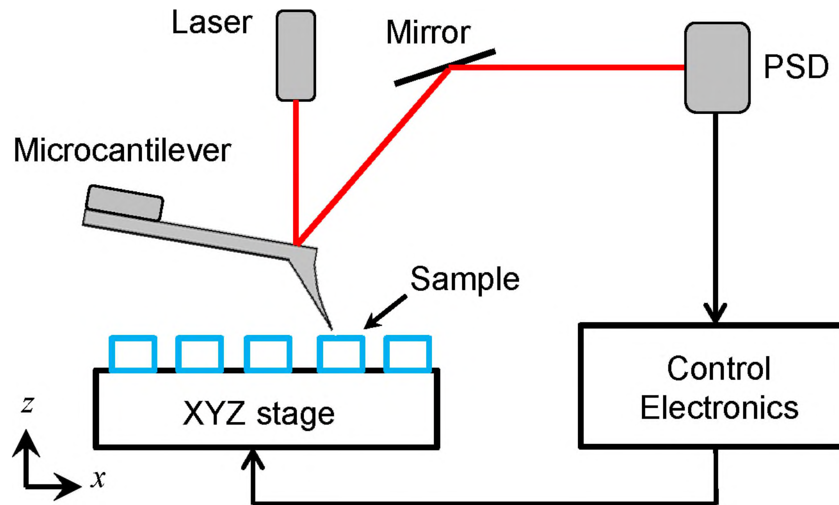

Figure 1.1. Schematic of an AFM.

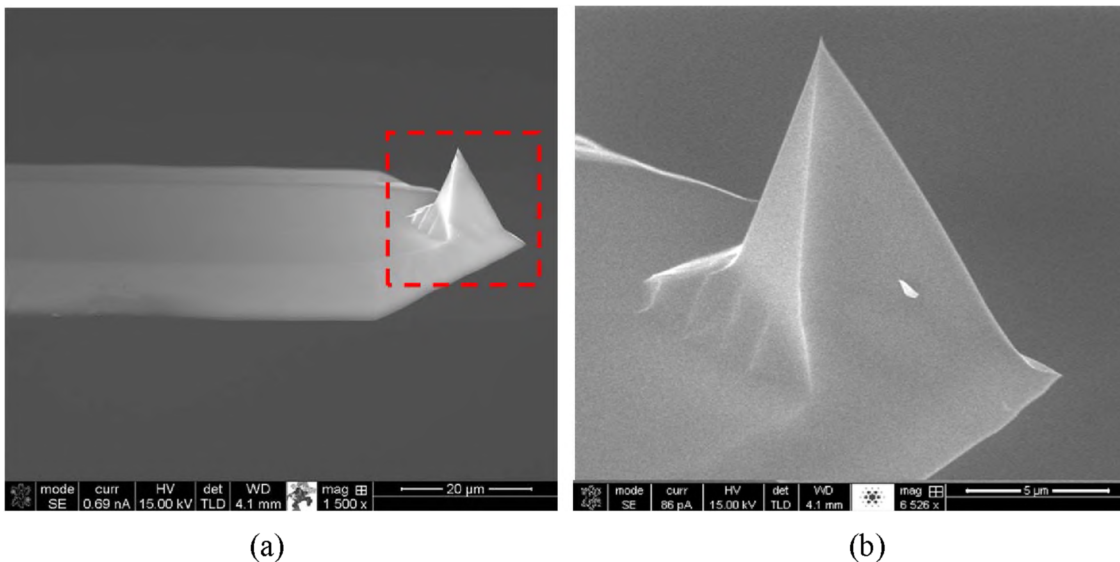

(a) (b)

Figure 1.2. SEM images of (a) Typical AFM microcantilever with a sharp tip at the end, (b) zoomed-in view of the AFM tip.

A unique aspect of AFM is it can be used to image a variety of samples at different ambient conditions. It can be used to image conductors [3], insulators [4] and biological samples [5] in near vacuum [6], air [7] and liquid [8] environments. Another interesting capability of AFM is that, apart from surface height measurement, it can map a host of different surface properties including mechanical stiffness [9], magnetic flux [10], electric charge distribution [11], and material composition [12]. This is achieved by operating the AFM in tapping mode [13], where the microcantilever is oscillated near its resonant frequency and the tip is made to gently tap the sample. The above mentioned properties are obtained by analyzing the different characteristics of probe deflection including higher harmonics and phase difference induced by tapping.

Besides the merits, there are some challenges associated with using the AFM. Unlike other microscopes, AFM takes several minutes to generate a single image, which would be especially disadvantageous if the sample phenomenon under study is dynamic. AFM imaging is also affected by tip wear [14], drift due to thermal expansion [15] of the AFM components, hysteresis and creep in the scanner [16]. These challenges are being addressed through better scanner design [17], improved tip-sample interaction modes [18], and advanced control methodologies [19].

1.1.1 Feedback Control in AFM. The important component of the AFM is the feedback controller that maintains a constant tip deflection by controlling the z-axis distance between the tip and the sample (Figure 1.3). Controlling the tip deflection, instead of operating in open-loop, avoids the effects of sensor saturation, nonlinearities in the stages, and thermal drift along the z-axis. Depending on the AFM mode, the tip deflection (contact mode) or the RMS of the tip oscillation (tapping mode) is regulated to

a constant set point value in the presence of sample height variations induced by raster scanning the sample. This method is called amplitude modulated AFM (AM-AFM). Other methods involving regulating the frequency (FM-AFM) [20] and phase (PM-AFM) [21] are used for special applications.

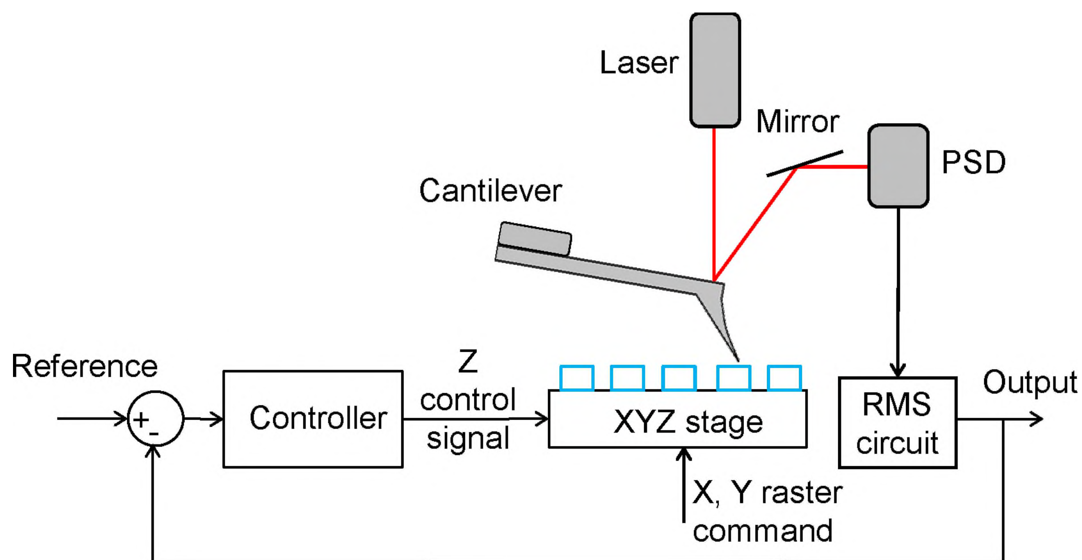

Figure 1.3. Illustration of a typical AFM control loop.

Typically PID controller is used for AFM control. However, a host of model-based approaches including nonlinear [22], adaptive [23], and robust [24] AFM control have been presented in the literature. Ideally if the controller completely rejects the sample height disturbance then the Z control signal becomes an accurate representation of the sample topography, and plotting it against the XY position of the probe would provide a 3D representation of the sample. However, the sample height disturbance acting on the loop is unknown, and this prevents asymptotic tracking of the sample.

Better tracking performance can be obtained by scanning the sample at a slower scan rate, but this affects the image throughput of the system.

1.1.2 Nanofabrication Using AFM. AFM is often referred to as a ‘nano-robot’, as it can be used for a variety of nano- manipulation and manufacturing applications. The tip which acts as a sensor in imaging applications can be used as an actuator enabling some of the macro scale processes to be carried out at the nanoscale level. Figure 1.4 shows some of the prominent processes that can be carried out using an AFM. One of the straightforward applications is nanomanipulation, where the tip is used to mechanically push or pull nanoparticles to obtain a certain arrangement. Alternatively, depending on the physical and chemical properties, certain particles can be picked-and-placed using chemical adhesion [25] or electric charge [26]. Apart from manipulation, the tip can also be used to add/remove materials to fabricate 2D structures. One of the prominent additive manufacturing processes is dip-pen nanolithography (DPN) [27], which involves immersing the AFM tip in solution of “ink” molecules and depositing on a substrate to print a desired pattern. DPN is a preferred manufacturing process because it is a ‘direct-write’ technique and does not require additional post processing. Moreover, a variety of materials including organic [28], inorganic [29], polymers [30] and biomolecules [31] can be printed with relative ease. Similarly, plowing is a material removal process which involves applying mechanical force to selectively remove material from the substrate to obtain a desired pattern.

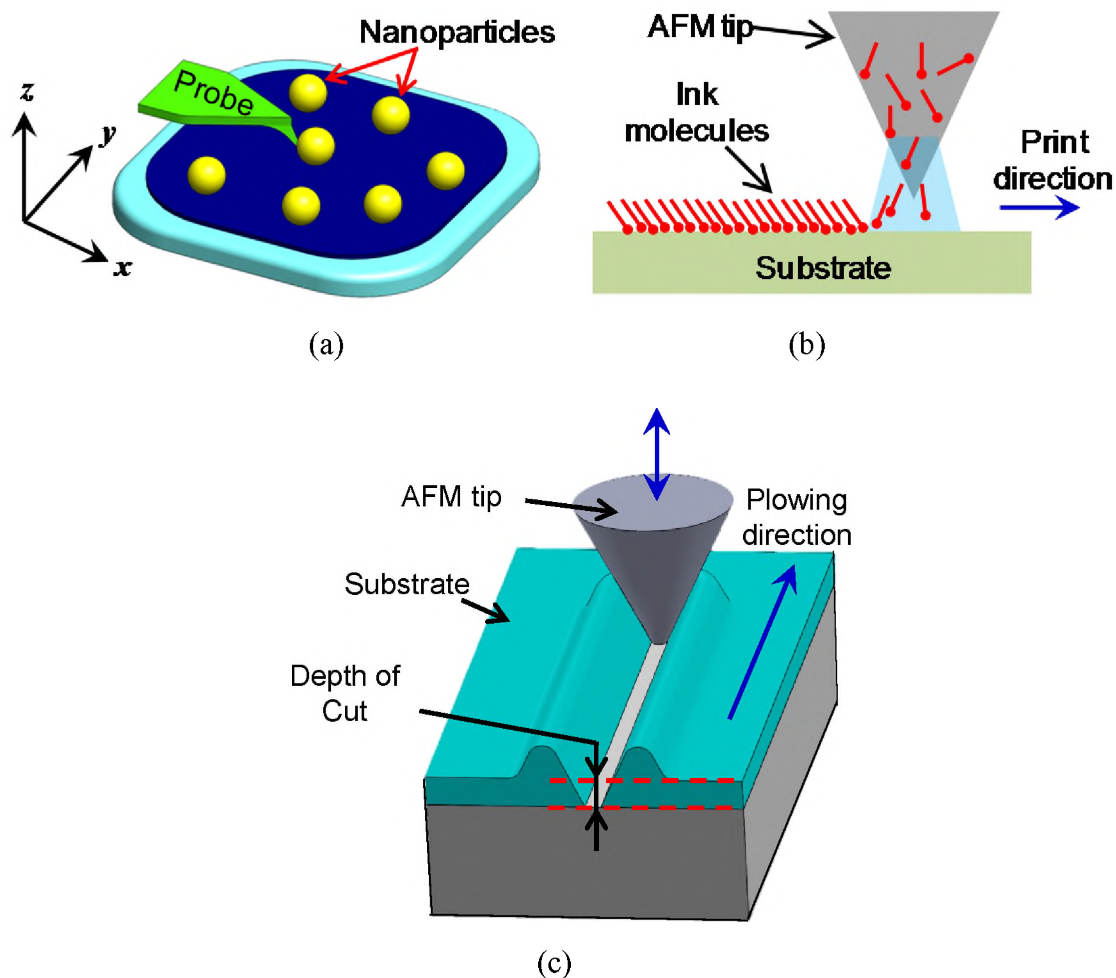

Figure 1.4. Illustration of (a) nanomanipulation using AFM probe, (b) dip-pen nanolithography process and (c) Nano plowing process.

Unlike imaging, nanofabrication processes are often carried out in open-loop. This is due to the lack of real-time feedback of the process. The AFM probe can be used either for fabrication or imaging, one at a time. This requires the user to switch between modes and follow a cumbersome trial-and-error approach until a desired result is achieved. Such an approach is less accurate and requires considerable user effort and expertise. Moreover, process uncertainties like varying sample properties and tip wear

affect the repeatability of the process. One way to overcome this challenge is to use AFMs which can actuate multiple probes. This would enable simultaneous fabrication and imaging, where one probe could carry out the fabrication process and other probes can follow the fabricating probe while imaging the process. The information from imaging can be used to correct the process in real-time.

1.1.3 Multi-Probe AFM Systems. Multi-probe systems have become an attractive proposition in recent times. While two probes [32-33] working in tandem provide unprecedented capabilities, AFMs with simultaneous actuation of up to four probes have been reported in the literature [34]. Some of these prominent multi-probe designs are shown in Figure 1.5. While some designs prefer conventional optical lever to accommodate standard cantilevers [32], other designs incorporate self-sensing probes [35] for compact packaging. The dual-probe configuration enables some unique applications including-

- Simultaneous imaging, where one probe can be used to image the topography while the other probe can be used to measure other physical properties [32] of the sample.
- Electrical measurements, where both the probes act as conductive ends to measure electrical properties like conductivity [33].
- Controlled manipulation, which involves using both the probes as gripper to pick-and-place nanoparticles to form 3D structures [36].
- Nanofabrication process control, where the imaging probe can provide real-time measurement of the process variables, like plow depth or DPN print thickness, as the process is carried out with the other probe.

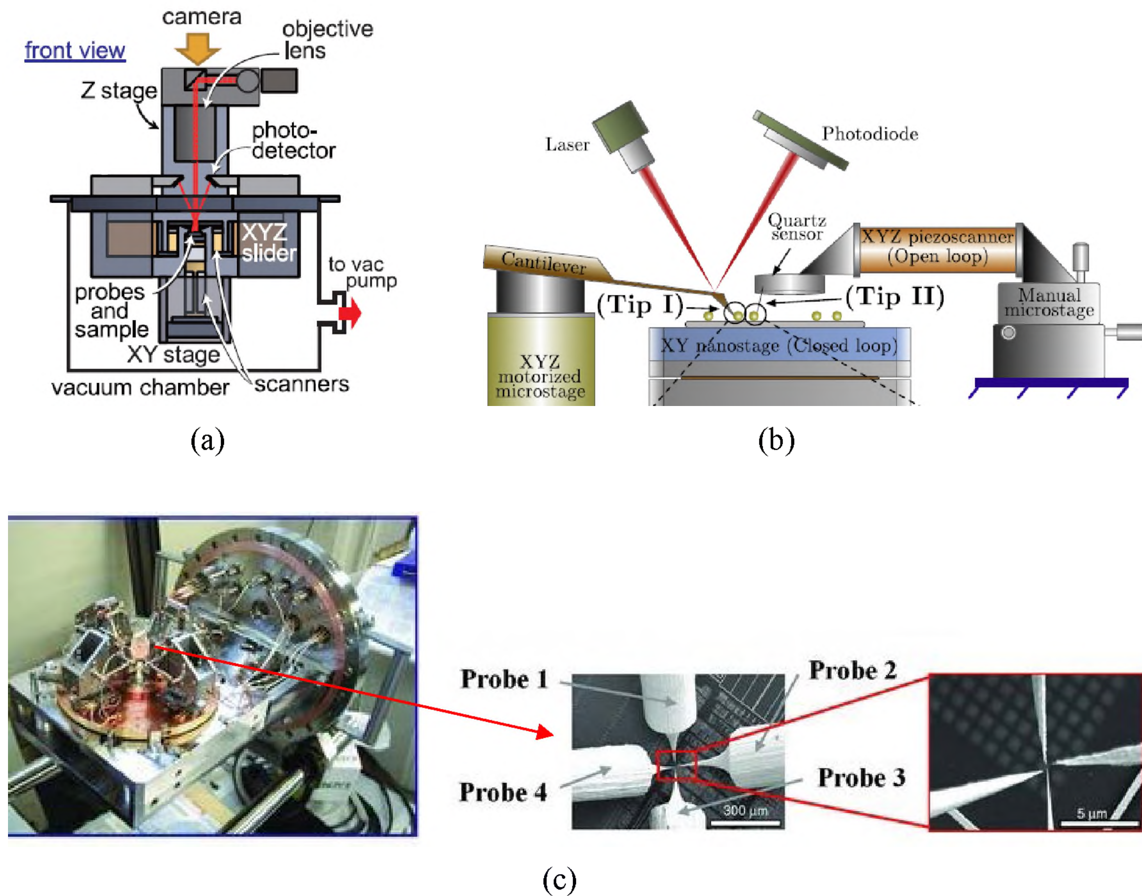

Figure 1.5. Multi-probe AFM systems presented in the literature. (a) A dual-probe AFM with two optical lever for each probe [33], (b) dual-probe design with a self-sensing AFM probe [35] and (c) a quadruple-probe AFM.

Apart from the hardware, the DP-AFM requires suitable feedback control design to carry out the above mentioned applications. Paper II presented in this dissertation introduces a DP-AFM design and provides a feedback control methodology to regulate plowing, a specific AFM process.

1.2 REPETITIVE CONTROL

Often in control applications, the reference or disturbance trajectories are periodic with a known period. Repetitive control (RC) [37-38] is a type of learning control capable of providing perfect tracking of periodic trajectories. It is based on internal-model principle [39], which implies that system can asymptotically track a reference if the model of the signal in included in the stable closed-loop system. A generalized periodic signal generator, composed of a FIFO buffer whose size equals a single period of the signal, serves this purpose. Repetitive controllers are widely used in disk drive systems [40-41] for track following, electric power systems [42] to reject harmonic noise effects, vibration isolation systems [43-44] to dampen periodic disturbances, and printers to remove repeating errors [45]. Though the basic principle remains the same, different variations of RC including robust [46] and adaptive [47-48] designs have been developed in recent years.

From the AFM perspective, raster scanning a typical sample induces a periodic-like disturbance in the feedback loop. Since these disturbances are not exactly periodic, a modified version of repetitive control that broadens the class of signals that can be tracked using RC framework is discussed in paper I. Apart from AFM, this controller can be used in applications where such periodic-like signals need to be tracked.

PAPER

I. A QUASI-REPETITIVE CONTROLLER FOR ACCURATE IMAGING IN ATOMIC FORCE MICROSCOPY

Muthukumaran Loganathan and Douglas A Bristow

ABSTRACT

While the classical Repetitive Controller provides a highly effective framework for asymptotic tracking of periodic signals, many signals of practical importance are quasiperiodic, i.e., are a function of periodic and aperiodic components. This paper focuses on modeling a class of quasiperiodic signals and deriving an internal-model based controller to asymptotically track/reject such signals. The quasiperiodic signals of interest are referred to as additive and multiplicative quasiperiodic. Additive (multiplicative) quasiperiodic signals are defined as signals that can be expressed as an algebraic sum (product) of periodic and polynomial signals. The resulting quasi-repetitive controller (QRC) is an extension of the classical repetitive controller, and asymptotic convergence is guaranteed by choosing an appropriate order of the controller based on the order of the quasiperiodic signal intended to be tracked. The QRC retains the plug-in structure of the repetitive controller, which enables it to be augmented with other feedback controllers. The motivation behind this work is the control of atomic force microscopy (AFM), where raster scanning non-planar and misaligned surfaces generates quasiperiodic disturbances in the feedback loop. Experimental AFM imaging results demonstrate that tracking performance can be increased by multiple-fold using the quasi-repetitive controller.

1. INTRODUCTION

Quasiperiodic signals, or signals expressed as a function of periodic and aperiodic components, are used to describe many phenomenon that may appear predominantly periodic, but with appreciable variation between different periods. Many of the physiological signals including heart beat [1], respiration [2], and speech [3] signals are often quasiperiodic. Another potential application of quasiperiodic signals, postulated here, is in Atomic Force Microscopy (AFM) [4]. In AFM, a sharp nano-sized tip raster scans a surface of interest to generate a nanoscale topographical image. Ideally, the sample is planar and aligned parallel to the scan plane, but in some instances parallel alignment is challenging and samples are non-planar [5]. Figure 1 shows a typical AFM sample and the temporal tracking signal resulting from raster scan. The raster profile induces a periodic triangular component, while the aperiodic components are from the orientation of the sample. Accurate AFM imaging necessitates accurate tracking of this signal.

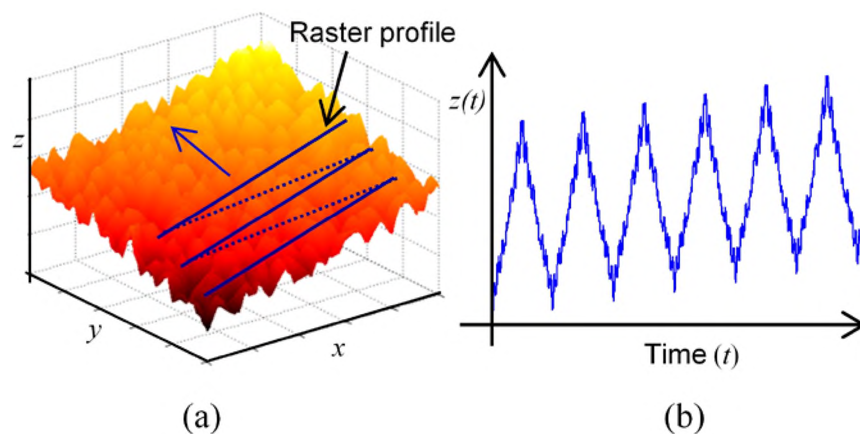

Figure 1. Illustration of (a) Typical AFM sample topography, and (b) The time-history of the height signal when the sample is raster scanned.

Methods for tracking quasiperiodic signals in the literature are based on adaptive control schemes using a first principles model to learn, and reject, the signal of interest. Applications including robotic assisted surgeries [6-7], vibration isolation [8] and noise cancellation [9] employ such methods for quasiperiodic signal tracking/rejection.

Alternatively, the repetitive control (RC) framework is widely utilized for high-performance tracking/rejection of periodic signals, such as in disk drive systems [10-11], power systems [12-13], motion control systems [14-15], and vibration control [16-17]. The RC framework is founded on the internal model principle (IMP) [18], which provides exceptionally accurate asymptotic tracking, provided the reference/disturbance signal is periodic with precisely known period. Extensions of the RC framework and design methods to uncertain periodic signal tracking have been developed [19-20], as well as adaptive methods for slowly-changing period [21]. More recently, in the related Iterative Learning Control field, new methods of embedding non-repeated trajectories in the control architecture have been developed [22-23], using an iteration-domain IMP.

This paper identifies a class of quasiperiodic signals that arise in AFM raster scanning of non-planar and misaligned samples. A quasi-repetitive controller (QRC) with "plug-in" [24] architecture is proposed that compactly captures the internal model of this class. Finally, experimental results in AFM imaging are evaluated on a misaligned sample and a glass fiber (non-planar) sample.

The remainder of the paper is organized as follows. The next section presents the formulation of generalized models for the class of quasiperiodic signals. Section 3 presents the quasi-repetitive controller design and implementation. Section 4 provides

experimental AFM imaging results comparing the performance of QRC against a PI controller. This is followed by conclusions in section 5.

2. QUASIPERIODIC SIGNAL MODELING

Modeling of additive and multiplicative quasiperiodic signals is described here. Figure 2 shows an example of these signal types. The analysis is carried out in discrete domain for ease of implementation. The additive quasiperiodic signals were introduced in [25], and are discussed here for completeness.

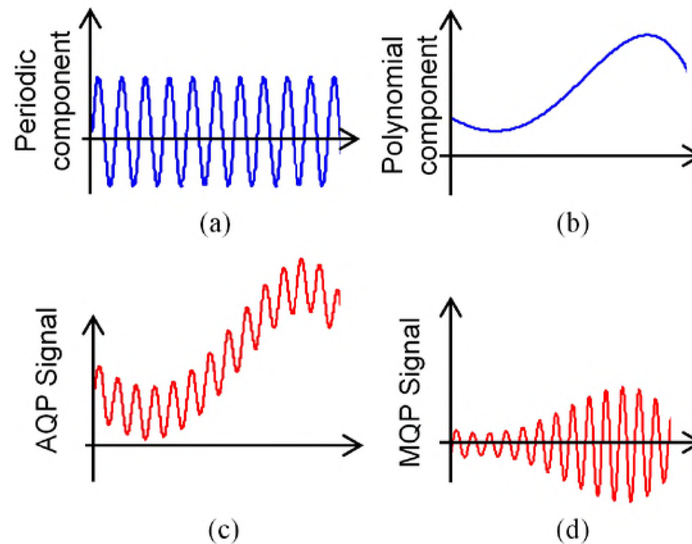

Figure 2. An illustrative example of (a) a periodic signal, (b) a polynomial signal, (c) an additive quasiperiodic (AQP) signal composed of (a) and (b), (d) a multiplicative quasiperiodic (MQP) signal composed of (a) and (b).

2.1. ADDITIVE QUASIPERIODIC SIGNALS

Consider an additive quasiperiodic signal $r_a(k)$ of the form

$$r_A(k) = r_p(k) + \gamma_0 + \gamma_1 k + \gamma_2 k^2 + \ldots + \gamma_n k^n, \quad (1)$$

where k is the discrete time step, $r_p(k)$ represents the periodic component with a sample period N, i.e. $r_p(k)= r_p(k+N)$ for the smallest integer N and all $k\geq 0$, and $\gamma_0, \gamma_1, ...\gamma_n$ are scalar coefficients of the polynomial component of order n. We refer to the order to the additive quasiperiodic signal as the polynomial order, n. The z-transform of (1) can be written as

$$R_A(z) = R_p(z) + \gamma_0 Z\{1\} + \gamma_1 Z\{k\} + ... + \gamma_n Z\{k^n\}, \tag{2}$$

where $Z\{\cdot\}$ represents the z-transform of the respective function. A generalized model [25] for a periodic signal of sample period N can be written as

$$R_p(z) = \frac{R_0(z)}{\left(1 - z^{-N}\right)}, \tag{3}$$

where $R_0(z)$ is described as

$$R_0(z) = r_p(0) + r_p(1) z^{-1} + ... + r_p(N-1) z^{-(N-1)}. \tag{4}$$

It can be noted that $R_0(z)$ exist as it is a finite series in z with first N samples of $r_p(k)$ as its coefficients. Furthermore, the z-transform of an nth order polynomial [25] can be represented as

$$Z\{k^n\} = \frac{F_n(z)}{(z-1)^{n+1}}, \tag{5}$$

for some rational polynomial $F_n(z)$ such that $F_n(z=1) \neq 0$. Substituting (3) and (5) in (2) yields

$$R_A(z) = \frac{R_0(z)}{\left(1 - z^{-N}\right)} + \frac{\gamma_0 F_0(z)}{z-1} + \frac{\gamma_1 F_1(z)}{(z-1)^2} + \ldots + \frac{\gamma_n F_n(z)}{(z-1)^{n+1}}. \tag{6}$$

It can also be observed that the denominator of the periodic component can be factorized as

$$\left(1^{-N} - z^{-N}\right) = (z-1)\sum_{j=1}^{N} z^{-j}. \tag{7}$$

So (6) can be simplified as

$$R_A(z) = \frac{R_0(z)(z-1)^n + \sum_{j=1}^{N} z^{-j} \sum_{m=0}^{n} \gamma_m F_m(z)(z-1)^{n-m}}{\left(1 - z^{-N}\right)(z-1)^n}. \tag{8}$$

Thus (8) is the generalized model of an nth order additive quasiperiodic signal with quasiperiod N (period of the periodic component). Equation (8), though complicated, does not have pole-zero cancellation because for $z = 1$, the numerator simplifies to $N\gamma_n F_n(1) \neq 0$. Moreover, the focus is on the characteristic equation of (8) since IMP requires the inclusion of it in the control design to guarantee asymptotic convergence.

2.2. MULTIPLICATIVE QUASIPERIODIC SIGNALS

The next set of signals of interest is the multiplicative quasiperiodic. A general mathematical description of multiplicative quasiperiodic signal, $r_m(k)$ can be written as

$$r_M(k) = r_p(k)\left[\gamma_0 + \gamma_1 k + \gamma_2 k^2 + \ldots + \gamma_n k^n\right], \tag{9}$$

where $r_p(k)$ is the periodic component with a sample period N and $\gamma_0, \gamma_1, \ldots \gamma_n$ are scalar coefficients of the polynomial component of order n. The signal can be expressed in z-domain as

$$R_M(z) = \gamma_0 R_p(z) + \sum_{j=1}^{n} \gamma_j Z\left\{k^j r_p\right\}. \tag{10}$$

The z-transform of $k^j r_p$ can be written as (proof in appendix)

$$Z\left\{k^j r_p\right\} = (-1)^j \sum_{i=1}^{j} \begin{Bmatrix} n \\ i \end{Bmatrix} z^i \frac{d^i R_p}{dz^i}. \tag{11}$$

Using this property (10) can be rewritten as

$$R_M(z) = \gamma_0 R_p(z) + (-1)^n \sum_{j=1}^{n} \gamma_j \sum_{i=1}^{j} \begin{Bmatrix} j \\ i \end{Bmatrix} z^i \frac{d^i R_p(z)}{dz^i}. \tag{12}$$

In order to evaluate $\frac{d^i R_p(z)}{dz^i}$, (3) is differentiated using the Leibniz rule which states that for differentiable functions f and g,

$$(fg)^{(k)} = \sum_{m=0}^{k} \begin{pmatrix} k \\ m \end{pmatrix} f^{(m)} g^{(k-m)}, \tag{13}$$

where $\begin{pmatrix} k \\ m \end{pmatrix}$ is the binomial coefficient and $^{(\cdot)}$ represents the order of differentiation.

Hence,

$$\frac{d^iR_p}{dz^i}=\frac{d^i}{dz^i}\left(R_0(z).\frac{1}{(1-z^{-N})}\right)$$
$$=\sum_{m=0}^{i}\binom{i}{m}\left[\frac{1}{(1-z^{-N})}\right]^{(m)}R_0(z)^{(i-m)}. \tag{14}$$

Substituting (14) in (12) yields

$$R_M(z)=\frac{\gamma_0R_0(z)}{(1-z^{-N})}+\ldots$$
$$\ldots(-1)^n\sum_{j=1}^{n}\gamma_j\sum_{i=1}^{j}\begin{Bmatrix}j\\i\end{Bmatrix}z^i\sum_{m=0}^{i}\binom{i}{m}\left[\frac{1}{(1-z^{-N})}\right]^{(m)}R_0(z)^{(i-m)}. \tag{15}$$

From (4), it can be observed that $R_0(z)$ takes the form

$$R_0(z)=\sum_{j=0}^{N}r_jz^{-j}, \tag{16}$$

where r_j is the magnitude of the periodic signal $r_p(k)$ corresponding single period. In practice, $N>>n$ which implies that the higher derivatives of $R_0(z)$ in (15) exist. Furthermore, since the focus is on the characteristic equation of the signal, (15) can be rewritten as

$$R_M(z)=\frac{\gamma_0R_0(z)}{(1-z^{-N})}+(-1)^n\sum_{j=1}^{n}\Big[\gamma_j\times$$
$$\sum_{i=1}^{j}\begin{Bmatrix}j\\i\end{Bmatrix}z^i\sum_{m=0}^{i}\binom{i}{m}\frac{F_m(z)}{(1-z^{-N})^{m+1}}R_0(z)^{(i-m)}\Big]$$
$$=\frac{\gamma_0R_0(z)}{(1-z^{-N})}+(-1)^n\sum_{j=1}^{n}\Bigg[\gamma_j\sum_{i=1}^{j}\begin{Bmatrix}j\\i\end{Bmatrix}\frac{z^i}{(1-z^{-N})^{i+1}}\times$$
$$\sum_{m=0}^{i}\binom{i}{m}F_m(z)(1-z^{-N})^{i-m}R_0(z)^{(i-m)}\Bigg], \tag{17}$$

where $F_m(z)$ is a rational polynomial in z that results from differentiating the term $(1-z^{-N})^{-1}$. Equation (17) can be further simplified as

$$R_M(z)=\frac{\gamma_0 R_0(z)}{(1-z^{-N})}+(-1)^n\sum_{j=1}^{n}\Bigg[\frac{\gamma_j}{(1-z^{-N})^{j+1}}\sum_{i=1}^{j}\begin{Bmatrix} j \\ i \end{Bmatrix} z^i$$

$$(1-z^{-N})^{j-1}\sum_{m=0}^{i}\binom{i}{m}F_m(z)(1-z^{-N})^{i-m}R_0(z)^{(i-m)}\Bigg]$$

$$=\frac{\gamma_0 R_0(z)}{(1-z^{-N})}+\frac{(-1)^n}{(1-z^{-N})^{n+1}}\sum_{j=1}^{n}\Bigg[\gamma_j(1-z^{-N})^{n-j}\times \qquad (18)$$

$$\sum_{i=1}^{j}\begin{Bmatrix} j \\ i \end{Bmatrix} z^i(1-z^{-N})^{j-i}\times$$

$$\sum_{m=0}^{i}\binom{i}{m}F_m(z)(1-z^{-N})^{i-m}R_0(z)^{(i-m)}\Bigg].$$

Equation (18) can be rewritten as

$$R_M(z)=\frac{\left[\gamma_0 R_0(z)(1-z^{-N})^n+(-1)^n\sum_{j=1}^{n}\left[\gamma_j(1-z^{-N})^{n-j}\times \sum_{i=1}^{j}\begin{Bmatrix} j \\ i \end{Bmatrix} z^i(1-z^{-N})^{j-i}\times \sum_{m=0}^{i}\binom{i}{m}F_m(z)(1-z^{-N})^{i-m}R_0(z)^{(i-m)}\right]\right]}{(1-z^{-N})^{n+1}}. \qquad (19)$$

Thus, (19) provides the generalized model for an nth order multiplicative quasiperiodic signal with quasiperiod N. Similar to the additive quasiperiodic model in (8), the numerator of the multiplicative quasiperiodic model is complicated, but again the focus is on the characteristic equation of the model, i.e. the denominator of (19), for control

design. The important characteristic to note is that for z=1, the numerator simplifies to $(-1)^n \gamma_n F_n(1) R_0(1) \neq 0$. This shows that there is no pole-zero cancellation.

2.3. AFM SAMPLE MODELING

The classes of signals described above are of significance in the control of atomic force microscopy (AFM). AFM renders high resolution nanoscale images by raster scanning a nano-sized tip across the surface of interest. Figure 3 illustrates the working principle of the AFM. The tip mounted on the free end of a microcantilever experiences change in deflection when there is a change in the surface height. Raster scan is enabled by loading the sample on a 3-axis nano positioner. The tip deflection is regulated to a constant value by controlling the z-axis position of the sample through a feedback controller. While scanning, the sample height acts as a disturbance on the feedback loop, and the control action applied to reject the disturbance is mapped against the position of the tip to generate a 3D topographical map of the sample.

While the objective is to image the 3D topography of the sample, the sample is often assumed to be grossly planar and aligned in the plane of the raster path. To the degree that the plane is misaligned, or potentially curved, it is common to fit a planar or higher order curve to the measured topography and subtract that curve from the image [26]. However, the dynamic errors created by tracking over the curve remain. Thus, accurate tracking of these large, gross geometries remains critically important in generating accurate images.

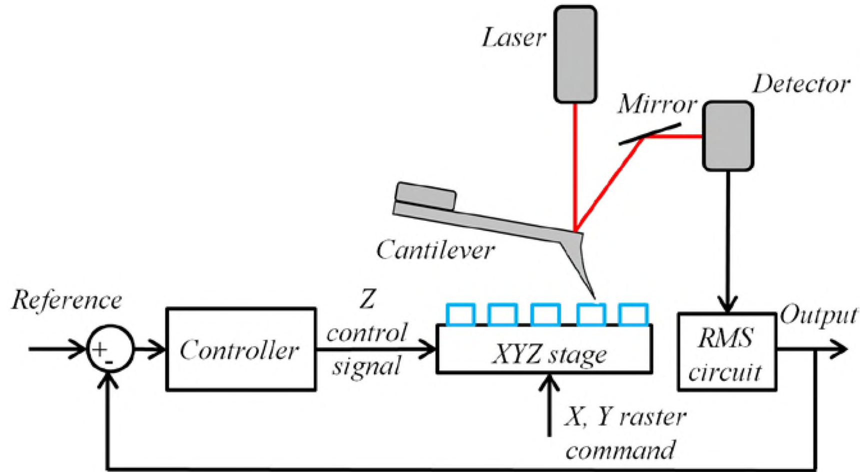

Figure 3. Illustration of an AFM control loop for regulating tip deflection. The sample height acts as the disturbance on the control loop while the tip scans the sample.

In order to understand the effect of the gross sample geometry on the tracking error, consider the sample as a 3D polynomial surface,

$$h(x,y) = d + \sum_{i=1}^{n_x} a_i x^i + \sum_{i=1}^{n_y} b_i y^i + \sum_{i=1}^{n_{xy}} c_i x^i y^{(n_{xy}-i)}, \tag{20}$$

where $h(x,y)$ is the surface height at a given spatial coordinate (x,y) with respect to the scanner frame, n_x, n_y, and n_{xy} are the polynomial orders, and a_i, b_i, c_i, and d are coefficients. The linear terms in h represent alignment of the raster plane to the sample plane, and higher order terms can represent more complex sample geometries such as glass rods [5] or cell surfaces [27].

Now consider a raster profile in X and Y represented by temporal signals $r_x(k)$ and $r_y(k)$. There are a variety of raster profiles used in AFM [28-29], such as the simple triangular profile shown in Figure 4. The following assumptions are made about the raster signals:

$r_x(k) \in \Omega_N$, where Ω_N is a set of periodic signals with sample period N.

$r_y(k)$ is linear with respect to time.

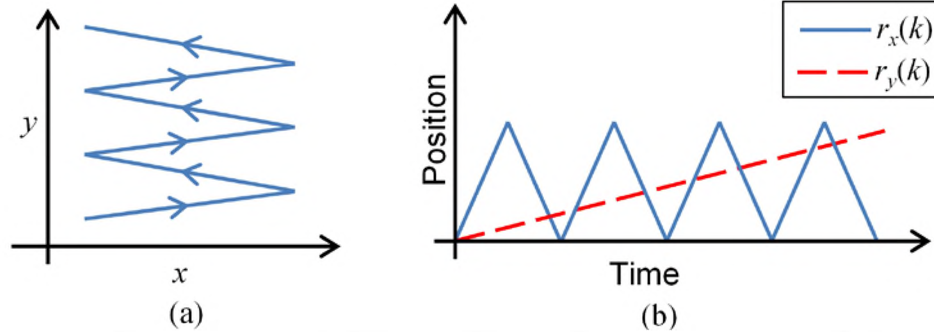

Figure 4. Typical raster pattern involved in scanning an AFM sample in (a) spatial domain, and (b) the time domain signals corresponding to individual axes to generate the raster pattern.

The temporal tracking signal can be obtained by substituting the raster profile functions into the sample topography (20) , resulting in,

$$h(k) = d + \sum_{i=1}^{n_x} a_i r_f{}^i + \sum_{i=1}^{n_y} b_i r_s{}^i + \sum_{i=1}^{n_{xy}} c_i r_f{}^i r_s{}^{(n_{xy}-i)}. \tag{21}$$

Periodic signals with the same sample period have closure under addition and multiplication, i.e. given a set of periodic signals (Ω_N) with same sample period, and $r_1, r_2 \in \Omega_N$ then $r_1 + r_2 \in \Omega_N$ and $r_1 \times r_2 \in \Omega_N$. This indicates that the first summation term in (21) is periodic with the same period as $r_f(k)$. Furthermore, it can be observed that the second summation term, being an algebraic sum of higher powers of the ramp signal, is a polynomial in k with the order n_y. So, the first three terms in (21) constitute an additive quasiperiodic signal with order n_y. The last summation term is composed of

product of periodic and polynomial signals, which indicates that it is a multiplicative quasiperiodic signal with order n_{xy}-1. Thus, the height disturbance in (21) is a combination of additive and multiplicative quasiperiodic signals. By designing an appropriate controller that can asymptotically track such signals, the AFM can be made image more accurately.

3. QUASI-REPETITIVE CONTROL DESIGN

The proposed quasi-repetitive controller is based on the internal model principle. The characteristic equations of the additive and multiplicative quasiperiodic signals are $\left(1-z^{-N}\right)(z-1)^n$ and $\left(1-z^{-N}\right)^{n+1}$ respectively. By including these models in the control design the signals can be tracked or rejected asymptotically. While including all the roots of both the characteristic equation as controller poles would ensure tracking, consider expanding the term $\left(1-z^{-N}\right)^{n+1}$ using (7), which yields

$$\begin{aligned}\left(1-z^{-N}\right)^{n+1} &= \left(1-z^{-N}\right)\left(1-z^{-N}\right)^{n} \\ &= \left(1-z^{-N}\right)(z-1)^{n}\left(\sum_{j=1}^{N} z^{-j}\right)^{n}.\end{aligned} \tag{22}$$

This shows that the characteristic roots of the MQP signal comprise the roots of the AQP signal as well. Thus, by including $\left(1-z^{-N}\right)^{n+1}$ as poles in the control design both additive and multiplicative quasiperiodic signals can be tracked.

3.1. CONTROLLER IMPLEMENTATION

Consider a generalized repetitive controller shown in Figure 5. *G(z)* and *K(z)* represent the plant and the baseline controller. *L(z)* is the learning filter, and is typically formulated as a zero-phase tracker [30] given by

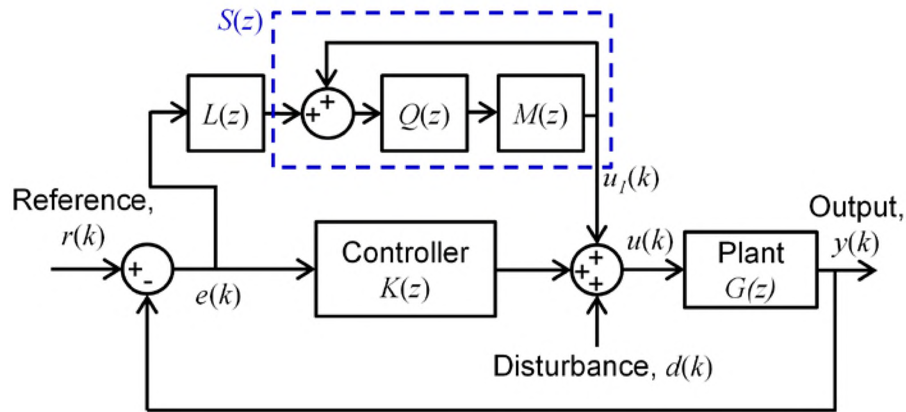

Figure 5. A generalized repetitive controller frame work. The highlighted section of the controller, *S*(*z*), represents the internal model of a periodic signal.

$$L(z) = k_r P^{-1}(z), \tag{23}$$

where k_r is the learning gain. The transfer function $P(z)$ is defined as

$$P(z) = \frac{G(z)}{1 + K(z)G(z)}. \tag{24}$$

$Q(z)$ is the Q-filter added to improve the robustness of the controller. It is generally a zero-phase, low pass filter. The block $M(z)$ is a FIFO buffer of size N ($M(z) = z^{-N}$) for a repetitive controller, which makes *S(z)* a periodic signal generator. To introduce higher

powers of $1-z^{-N}$, the block $M(z)$ is modified to have multiple FIFO buffers connected as shown in Figure 6. Such a structure can be mathematically represented as

$$M(z)=\sum_{m=1}^{p}a_m z^{-mN}, \quad (25)$$

where p is the number of N-length FIFO buffers and represents the order of the quasi-repetitive controller, and a_m are suitable gains with which the outputs of the buffers are scaled. To simplify the analysis consider $Q(z)=1$. The transfer function of the plug-in repetitive component from $e(k)$ to $u_1(k)$ is

$$\frac{U_1(z)}{E(z)}=\frac{L(z)\sum_{m=1}^{p}a_m z^{-mN}}{1-\sum_{m=1}^{p}a_m z^{-mN}}. \quad (26)$$

In order to choose appropriate values for a_m to obtain higher powers of $\left(1-z^{-N}\right)$, consider the binomial expansion of $\left(1-z^{-N}\right)^p$ which can be written as

$$\left(1-z^{-N}\right)^p=1-\sum_{m=1}^{p}\hat{a}_m z^{-mN} \quad (27)$$

where

$$\hat{a}_m=(-1)^{m-1}\binom{p}{m} \text{ for } m=1,2,\ldots p$$

So, setting $a_m=\hat{a}_m$ yields

$$\frac{U_1(z)}{E(z)} = \frac{L(z)\sum_{m=1}^{p} \hat{a}_m z^{-mN}}{\left(1 - z^{-N}\right)^p}. \tag{28}$$

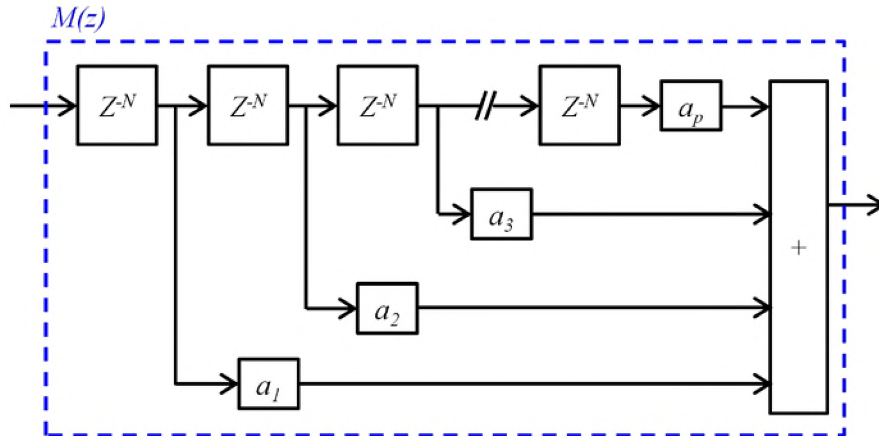

Figure 6. Multi-buffer internal model structure for a quasiperiodic signal.

By choosing $p \geq n+1$, i.e. setting the order of the quasi-repetitive controller higher than the order of the quasi-periodic signal, asymptotic tracking can be guaranteed. As a special case, it can be noted QRC of order p=1 is a generic repetitive controller which can track periodic signals (*n*=0). Different gain values $\hat{a}_m$ for different order of quasi-repetitive control (*p*) is tabulated Table 1.

Table 1. Gain Values for QRC up to Order 4

RC Order (p)	$\hat{a}_1$	$\hat{a}_2$	$\hat{a}_3$	$\hat{a}_4$
1	1	0	0	0
2	2	-1	0	0
3	3	-3	1	0
4	4	-6	4	-1

Remark: A control structure identical to quasi-repetitive control (QRC) has been previously presented in works by Steinbuch et al [31]. Though the control structure is similar, the goal of the design is different. While Steinbuch et al have applied this control structure to improve robustness to time-period variations, the same structure here is used to expand the type of signals that can be tracked using repetitive control architecture.

4. EXPERIMENTAL RESULTS & DISCUSSION

The quasi-repetitive controller was implemented on a custom AFM using Labview. The learning filter design involved identifying and inverting the plant dynamics. The learning gain k_r was set to 0.8. The Q-filter was chosen to be a zero-phase, low pass FIR filter. A PI controller was chosen as the baseline controller to which the QRC was augmented. As described in section III, the criteria for a pth-order QRC to track an nth-order quasiperiodic signal (additive or multiplicative) is $p \geq n+1$.

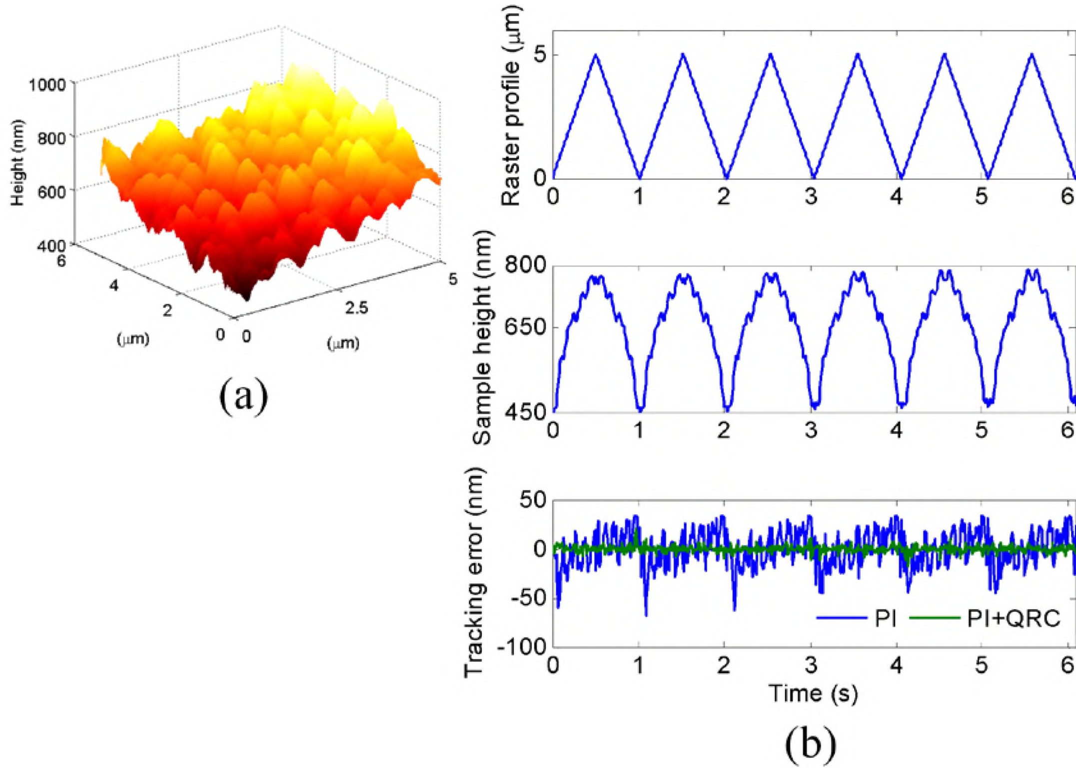

Figure 7. Experimental results corresponding to imaging a Magnetite sample. (a) 3D image of the sample is inclined due to the misalignment between the sample and the raster plane, (b) Raster profile of the scanner, sample height, and the tracking error of PI and PI+QRC schemes corresponding to 6 raster cycles.

To track an AFM sample as described in (20), which is a combination of additive quasiperiodic signal of order n_y and multiplicative quasiperiodic signal of order n_{xy}-1, QRC with $p \geq \max(n_y, n_{xy} - 1) + 1$ would provide asymptotic convergence. Two samples of varying topography were imaged using PI controller and PI+QRC combination. First, a planar sample of Magnetite was imaged. Such a sample can be approximated as (21), with n_x=n_y=1 and n_{xy}=0. So, the order of QRC was set to 2. The sample was scanned at 1 Hz using both PI and PI+QRC schemes. Figure 7(a) shows the 3D topography of the

Magnetite sample generated using the PI controller. Figure 7(b) shows the raster scan profile, temporal height signal and the tracking error of PI and PI+QRC for limited cycles of raster scans.

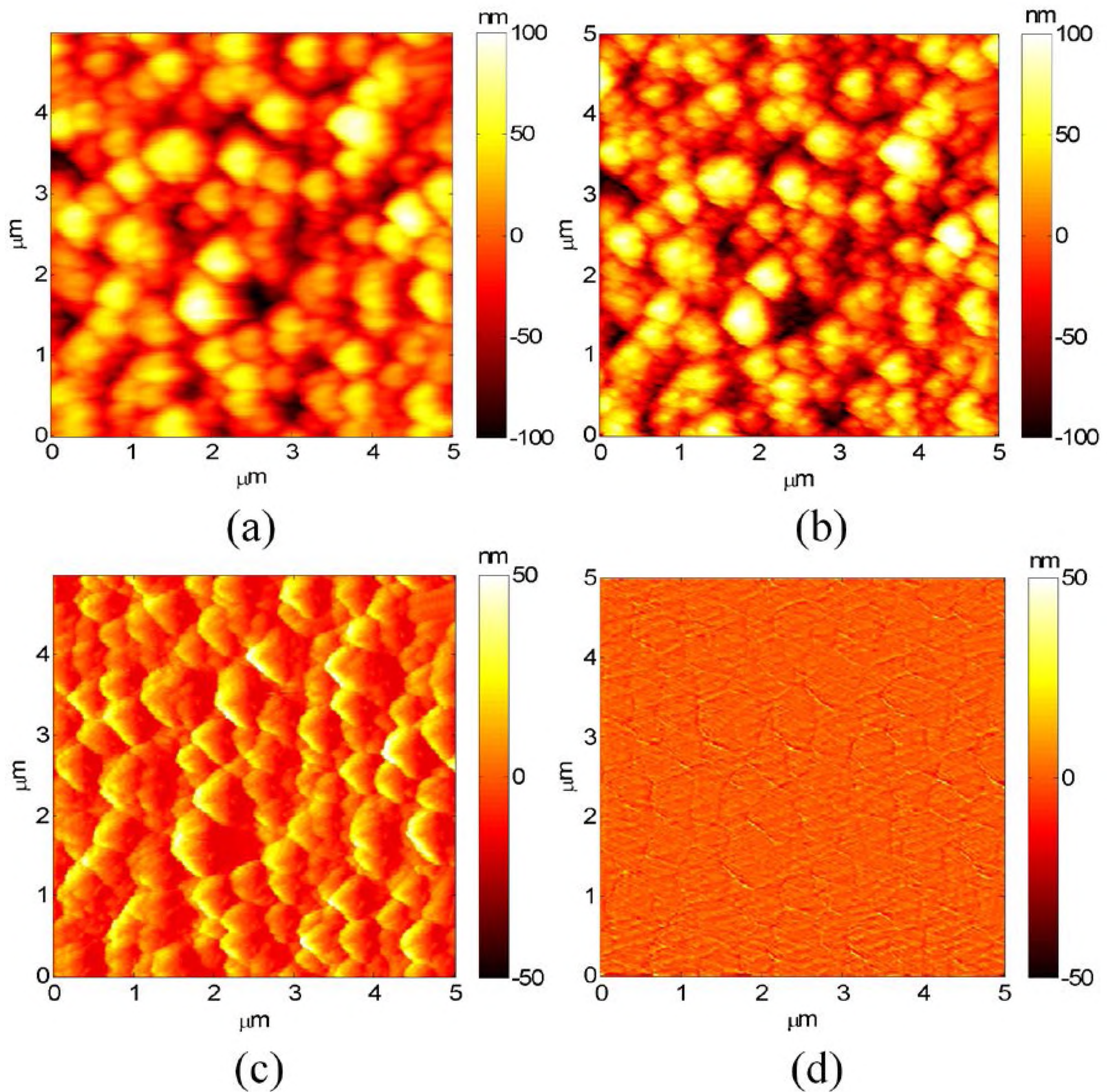

Figure 8. Magnetite sample imaged using a (a) PI controller and (b) PI+QRC controller. The tracking error of PI (PI_{RMS} = 12.3 nm) and PI +QRC (QRC_{RMS}= 3.9 nm) schemes are plotted in spatial domain in (c) and (d).

The misalignment between the sample and raster plane is evident in Figure 7(a) and it affects the tracking performance of the PI controller. It can be observed that the PI tracking error is in itself quasiperiodic in nature. As a standard practice the image in Figure 7(a) is flattened by subtracting the best plane fit from the image data. Figure 8 shows the flattened AFM image and the tracking error obtained by scanning the same location on the sample using PI and PI+QRC schemes. The tracking errors were quantified by calculating their RMS across the entire scan range. The RMS of the QRC tracking error (QRC_{RMS} = 3.9 nm) was approximately 3 times smaller when compared to the PI tracking error (PI_{RMS} = 12.3 nm). The second sample considered for imaging was a glass rod with a cylindrical topography with 150 μm diameter. It was raster scanned along its longitudinal axis with 1 Hz scan rate. Assuming X-axis is the fast raster axis, such a cylindrical topography along with the sample plane misalignment would have circular profile along X-direction and linear profile along Y-direction. Thus when represented in the form given in (21), it can be approximated with n_y=1 and n_{xy}=0. Note that the order of the profile along the X-direction does affect the QRC order required for asymptotic tracking. Thus, QRC with order, p=2 was chosen. Figure 9 shows the images of the glass rod sample scanned along its longitudinal axis using both PI and PI+QRC controllers. Again, QRC (QRC_{RMS} = 5.2) provides approximately 5 times better tracking performance compared to PI controller (PI_{RMS} = 28.1). Apart from the error images, the improvement in tracking performance is also visually evident in the sample topography images. Image generated by PI controller has sharp discontinuities, which are caused by sensor saturation due to poor tracking. This does not occur in QRC owing to superior tracking.

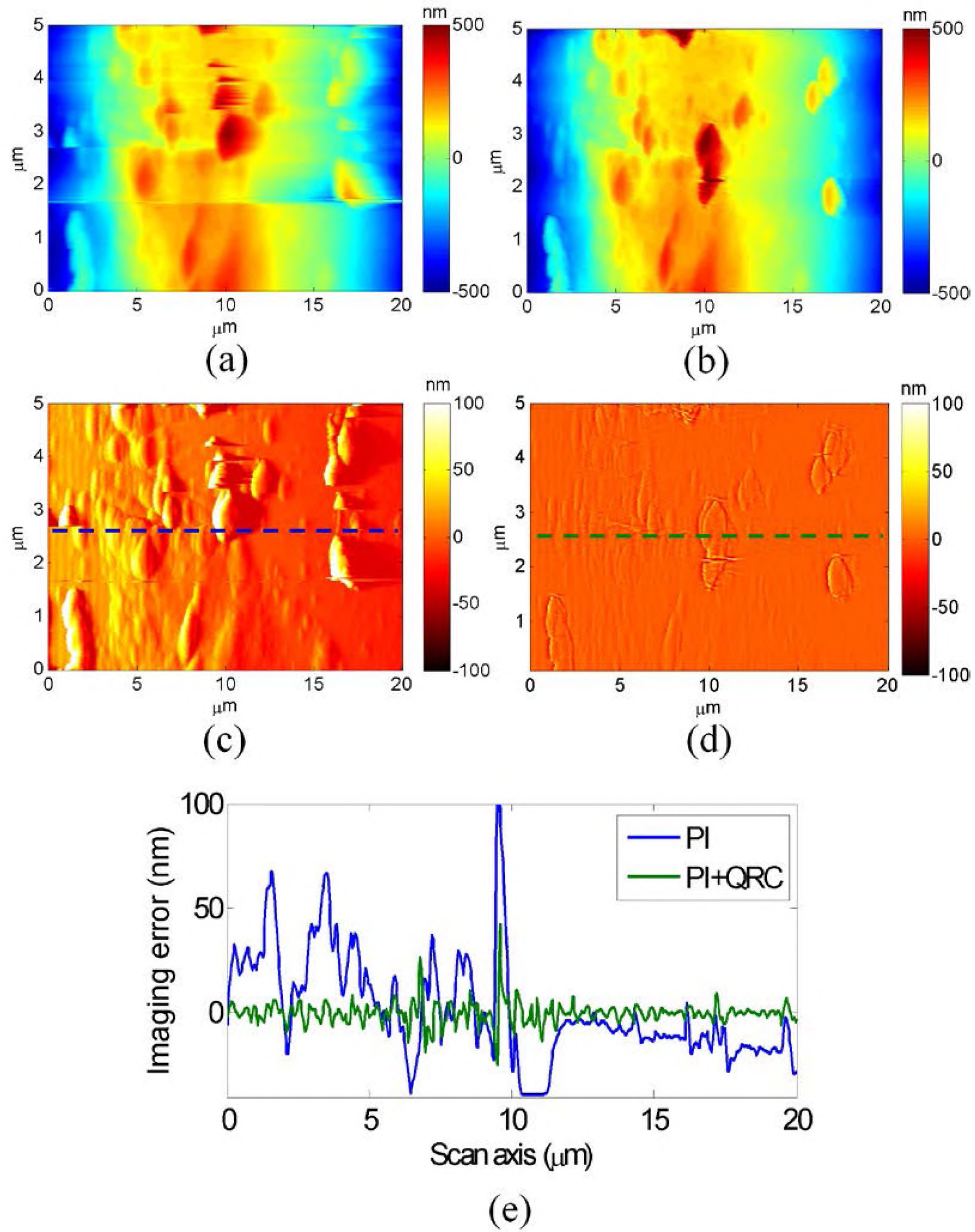

Figure 9. Image of a glass rod sample obtained using (a) PI controller and (b) PI+QRC combination. The tracking error of PI (PI_{RMS} = 28.1 nm) and PI +QRC (QRC_{RMS}= 5.2 nm) schemes are plotted in spatial domain in (c) and (d). Comparison of tracking error of PI and PI+QRC at the dotted line marked in (c) and (d) is shown in (e).

5. CONCLUSIONS

Conventional repetitive controller framework, which enables perfect periodic signal tracking, was extended to track a broader set of quasiperiodic signals. A generalized model of signals that can be written as linear combinations of periodic and polynomial signals were derived in discrete domain and a quasi-repetitive controller was formulated based on internal model principle. One application that can benefit from QRC is atomic force microscopy. It was analytically shown how raster scanning a 3D polynomial surface induces quasiperiodic disturbances in the feedback loop and how, with minimal knowledge of the surface geometry, asymptotic tracking can be obtained. AFM imaging was performed with the developed controller and its performance was compared to a PI controller. Experimental results indicate superior tracking by QRC which translates into more accurate surface images.

REFERENCES

[1] D. Cyrill , J. McNames, and M. Aboy, "Adaptive comb filters for quasiperiodic physiologic signals." In *Engineering in Medicine and Biology Society, 2003. Proceedings of the 25th Annual International Conference of the IEEE*, *3*, pp. 2439-2442, 2003.

[2] C. N. Riviere, A. Thakral, I. I. Iordachita, G. Mitroi, and D. Stoianovici, "Predicting respiratory motion for active canceling during percutaneous needle insertion." In *Engineering in Medicine and Biology Society, 2001. Proceedings of the 23rd Annual International Conference of the IEEE*, *4*, pp. 3477-3480, 2001.

[3] B. Yegnanarayana, C. d'Alessandro, and V. Darsinos, "An iterative algorithm for decomposition of speech signals into periodic and aperiodic components." *IEEE Transactions on Speech and Audio processing*, *6*, pp. 1-11, 1998.

[4] G. Binnig and C. F. Quate, “Atomic Force Microscope,” *Physical Review Letters*, *56(9)*, pp. 930-933, 1986.

[5] S. Chen, Q. Yang, R. K. Brow, K. Liu, K. A. Brow, Y. Ma, and H. Shi, “In vitro stimulation of vascular endothelial growth factor by borate-based glass fibers under dynamic flow conditions.” *Materials Science and Engineering: C*, *73*, pp.447-455, 2017.

[6] C. N. Riviere, R. S. Rader, and N. V. Thakor, "Adaptive cancelling of physiological tremor for improved precision in microsurgery." *IEEE Transactions on Biomedical Engineering, 45(7)*, pp. 839-846, 1998.

[7] E. E Tuna, T. J. Franke, O. Bebek, A. Shiose, K. Fukamachi, and M. C. Cavusoglu, “Heart motion prediction based on adaptive estimation algorithms for robotic-assisted beating heart surgery.” *IEEE Transactions on Robotics*, *29*(1), pp.261-276, 2013.

[8] Y. Xu, M. de Mathelin, and D. Knittel, “Adaptive rejection of quasi-periodic tension disturbances in the unwinding of a non-circular roll.”, In *American Control Conference, 5*, pp. 4009-4014, 2002.

[9] M. Sambur, "Adaptive noise canceling for speech signals." *IEEE Transactions on Acoustics, Speech, and Signal Processing, 26(5)*, pp. 419-423, 1978.

[10] B. A. Francis and W. M. Wonham, “The internal model principle for linear multivariable regulators,” *Applied Mathematics and Optics*, *2*, pp. 170-194, 1975.

[11] K. K. Chew and M. Tomizuka, "Digital control of repetitive errors in disk drive systems," *Proceedings of the American Control Conference*, pp. 540-548, 1990.

[12] J. Moon, M. Lee and M. Chung, "Repetitive control for the track-following servo system of an optical disk drive," *IEEE Transactions on Control systems Technology*, *6(5)*, pp. 663-670, 1998.

[13] Y.Y. Tzou, R. S. Ou, S. L. Jung, and M. Y. Chang, "High-performance programmable AC power source with low harmonic distortion using DSP-based repetitive control technique." *IEEE Transactions on Power Electronics*, *12(4)*, pp.715-725, 1997.

[14] R. Grino, R. Cardoner, R. Costa-Castelló, and E. Fossas, "Digital repetitive control of a three-phase four-wire shunt active filter." *IEEE Transactions on Industrial Electronics*, *54*(3), pp.1495-1503, 2007.

[15] D. H. Kim and T. C. Tsao, "Robust performance control of electrohydraulic actuators for electronic cam motion generation," *IEEE Transactions on Control Systems Technology*, *8(2)*, pp. 220-227, 2000.

[16] B. S. Kim, J. Li, and T. C. Tsao, "Two-parameter robust repetitive control with application to a novel dual-stage actuator for noncircular machining," *IEEE Transactions on Mechatronics*, 9(4), pp. 644-652, 2004.

[17] G. Hilllerstrom, "Adaptive suppression of vibrations- a repetitive control approach," *IEEE Transactions on Control Systems Technology*, 4(1), pp. 72-77, 1996.

[18] S. Daley, J. Hatonen, and D. H. Owens, "Active vibration isolation in a "small spring" mount using a repetitive control approach," *Control Engineering Practice*, 14(9), pp. 991-997, 2006.

[19] E. Kurniawan, Z. Cao, and Z. Man, "Design of robust repetitive control with time-varying sampling periods," *IEEE Transactions on Industrial Electronics,* 61(6), pp. 2834-2841, 2014.

[20] H. G. Dotsch, H. T. Smakman, P. M Van den Hof and M. Steinbuch, "Adaptive repetitive control of a compact disc mechanism," *Proceedings of the 34th IEEE Conference on Decision and Control*, 2, pp. 1720-1725, 1995.

[21] G. Hillerstrom, "Adaptive suppression of vibrations-a repetitive control approach," *IEEE Transactions on Control Systems Technology*, *4*(1), pp.72-78, 1996.

[22] C. Liu, J. Xu, and J. Wu, "Iterative learning control with high-order internal model for linear time-varying systems," *American Control Conference,* pp. 1634-1639, 2009.

[23] C. Yin, J. Xu, and Z. Hou, "On iterative learning control design for tracking iteration-varying trajectories with high-order internal model," *Journal of Control Theory and Applications*, 8(3), pp. 309-316, 2010.

[24] T. C. Tsao, and K. K. Chew, "Analysis and synthesis of discrete-time repetitive controllers," *Journal of Dynamic Systems, Measurement, and Control, 111*, p.353, 1989.

[25] M. Loganathan, and D. A. Bristow, "Quasi-repetitive control for fast and accurate atomic force microscopy," *American Control Conference,* pp. 360-365, 2016.

[26] V. J. Morris, A. R. Kirby, and A. P. Gunning, " Basic Principles" in *Atomic force microscopy for biologists* London: Imperial College Press, 2009, pp. 70-73.

[27] J. Rheinlaender, N. A. Geisse, R. Proksch, R. and T. E. Schäffer, "Comparison of scanning ion conductance microscopy with atomic force microscopy for cell imaging," *Langmuir*, *27*(2), pp.697-704, 2010.

[28] D. Y. Abramovitch, S. B. Andersson, L. Y. Pao, and G. Schitter, "A tutorial on the mechanisms, dynamics, and control of atomic force microscopes," *American Control Conference,* pp. 3488-3502, 2007.

[29] P. I. Chang, P. Huang, J. Maeng, and S. B. Andersson, "Local raster scanning for high-speed imaging of biopolymers in atomic force microscopy," *Review of scientific instruments*, *82*(6), pp. 063703, 2011.

[30] M. Tomizuka, T. Tsao, K. Chew, "Discrete-time domain analysis and synthesis of repetitive controllers," *American Control Conference,* pp.860-866, 1988.

[31] M. Steinbuch, "Repetitive control for systems with uncertain period-time," *Automatica,* 38(12), pp. 2103-2109, 2002.

II. DESIGN AND CONTROL OF A DUAL-PROBE ATOMIC FORCE MICROSCOPE

Muthukumaran Loganathan, Ayad Al-Ogaidi, and Douglas A. Bristow

ABSTRACT

Current atomic force microscopes (AFM) support single-probe operation, in which one nano-sized tip enables versatile operations, such as surface imaging, nanomanipulation, and nanomanufacturing, to be performed, although one at a time. Some AFM operations involve switching between imaging and the operational mode which is cumbersome, challenging and limiting, particularly when different probe geometries are preferred for each mode. This paper presents a new dual-probe atomic force microscope (DP-AFM) that has two independent probes operating in a common workspace. Such a setup enables two AFM operations to be carried out simultaneously. For instance, one probe can be used to image while the other probe performs one of the many tip based processes. The hardware and software design involved in developing the DP-AFM is discussed in detail. Furthermore, to demonstrate the capability of dual-probe arrangement, a controller is developed for real-time plowing depth control where one probe is used to plow the surface while the other is used to image the plow profile, thus enabling real-time feedback control of the AFM plow process. Experimental results show that the plow depth can be regulated with nanometer-level accuracy.

1. INTRODUCTION

Since its invention in 1986 [1], the atomic force microscope (AFM) has evolved from being a basic surface imaging tool to a fundamental nanomanufacturing tool. The AFM is widely used for nanoscale imaging, as it can image a variety of samples ranging from conductors, insulators [2], and biological specimens [3], in different ambient conditions including air, liquid [4], and vacuum [5]. Apart from surface topography, elastic [6], electrostatic [7] and magnetic properties [8] can be measured with sub-nanometer spatial resolution. This is made possible by a nano-sized tip, often mounted on a free end of a cantilever beam, which senses atomic forces with high resolution. Apart from sensing, the AFM tip can also act as an actuator to perform nanomanipulation and manufacturing tasks. In nanomanipulation, the tip is used to apply mechanical force to push, pull or pick-and-place individual nanoparticles in a controlled manner through force feedback [9-10]. Nanomanufacturing involves adding or removing material using the tip to fabricate 2D/3D structures. For example, dip-pen nanolithography [11-12] is one of the bottom-up manufacturing processes where the AFM tip is used to deposit 'ink' molecules of interest on a substrate to print a desired pattern. Similarly, plowing [13] is a subtractive process where the tip is used to selectively remove material off the substrate through mechanical means. Local oxidation [14] and nanomilling [15] are some of the other prevalent tip-based nanomanufacturing processes.

Despite the versatility of the single-probe configuration, there are significant limitations. First, single-probe AFM can either perform imaging or nano manipulation/manufacturing, one at a time. Since imaging cannot be performed during the fabrication process, real-time feedback of the process is challenging, whereas

performing the process in open-loop without real-time feedback limits the accuracy. Second, current fabrication methods involve alternating between imaging mode and the fabrication mode until a certain goal is accomplished. This trial-and-error aspect is inefficient as it often requires a considerable amount of operator time, effort, and expertise. Alternatively, efforts have been made to automate processes like nanomanipulation [16-17]. However, automation is not much of help in cases where different modes require different probes. Third, there is a limitation to the complexity of the part that can be fabricated using single-probe AFM. Simple 2D nanoparticle manipulation and plowing of basic 2D geometrical shapes, using single-probe AFM, have been reported in the AFM literature. However, complex 3D pick-and-place manipulation or complicated plowing profiles are almost impossible to achieve using single-probe configuration

One approach to overcome the aforementioned limitations is to enable simultaneous actuation and sensing by having two probes working in tandem, in a common workspace. One of the probes can perform imaging while the other probe can engage in one of the many manipulation or manufacturing tasks. Dual-probe AFM setup with different configurations [18-19] has been of recent interest to the nanotechnology community. Some unique applications like simultaneous imaging of two physical properties [20], electrical characterization of nano-rods [21], and 3D pick-and-place [22] of microspheres that are impossible with single-probe AFM, have been successfully demonstrated using DP-AFM. This paper presents a new modular dual-probe AFM capable of independently actuating two probes simultaneously in a common workspace. Design and signal processing for this complex mechatronics system is presented. A real-

time control algorithm for this system is developed and applied in the AFM plowing process.

The remainder of the paper is organized as follows. In the next section, a DP-AFM description including hardware and software design is presented. Section 3 discusses calibration challenges pertaining to the DP-AFM and proposes procedures to address them. Section 4 presents a unique application of plowing process control which involves controlling the plow depth in real-time using the DP-AFM. Experimental results highlighting the challenges of open-loop plowing and the effectiveness of closed-loop plowing are presented in Section 5 followed by conclusion in Section 6.

2. SYSTEM DESIGN

An integral component of an AFM system is the nano-sized tip that acts as an end-effector to perform various operations. Having more than one tip operating simultaneously provides better control over the workspace. For example, micro or nanoparticles can be manipulated using two opposing tips by performing a more controlled pick-and-place action, compared to less efficient push or pull action using a single probe. The DP-AFM is designed to have two opposing probes, as illustrated in Figure 1, operate in a common workspace.

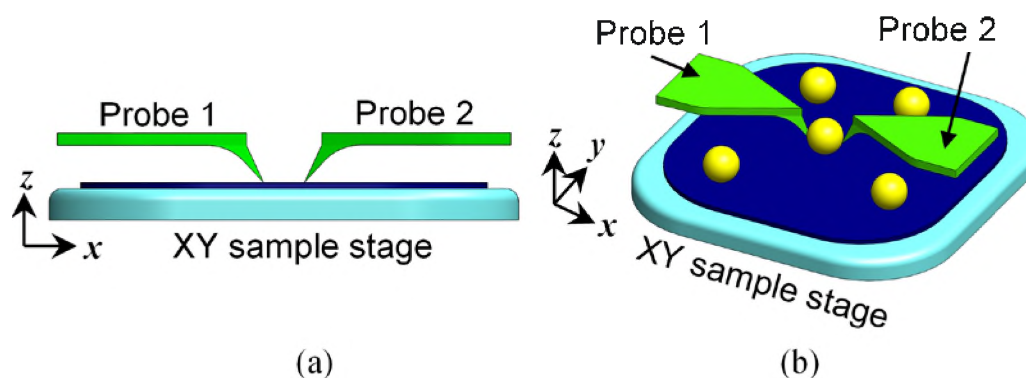

Figure 1. Illustration of (a) opposing dual probe configuration with top visual probes and (b) manipulation application using the two opposing probes.

While conventional AFM probes, whose tips are not visible from the top, can be used in a dual probe arrangement, probes with protruding tip, as shown in Figure 1, provide a distinct advantage allowing multiple probes to approach one another with zero offset between their tips. Each probe can be operated individually and is capable of supporting standard AFM operations and cantilevers when applicable. Both the probes can be operated in tapping or contact mode depending on the application. The design also incorporates a standard optical lever for probe displacement detection so that commercial cantilevers made for single-probe AFM can be still be accommodated.

The DP-AFM setup consists of two independent 3-axis nano stages (PI PicoCube P-363) for actuating the probes, and a separate 3-axis nano stage (PI Hera P-621) for sample actuation. The probe stages have 5 μm range in all the three directions with a resolution of 0.1 nm and 1000 Hz bandwidth. This effectively provides 5x5x5 μm^3 of workspace where both the probes can operate. The sample stage has 100 μm range along the sample plane (X & Y axes), and 50 μm range normal to the sample (Z axis). The XY

stages have a resolution of 0.2 nm and 600 Hz bandwidth, while the Z stage has 0.1 nm resolution and 800 Hz bandwidth. Each probe has its own optical lever setup i.e. dedicated laser source (Schäfer + Kirchoff 51nanoFCM) and position-sensitive photodetector (PSD) (MAYPA tech OPS-40) pair.

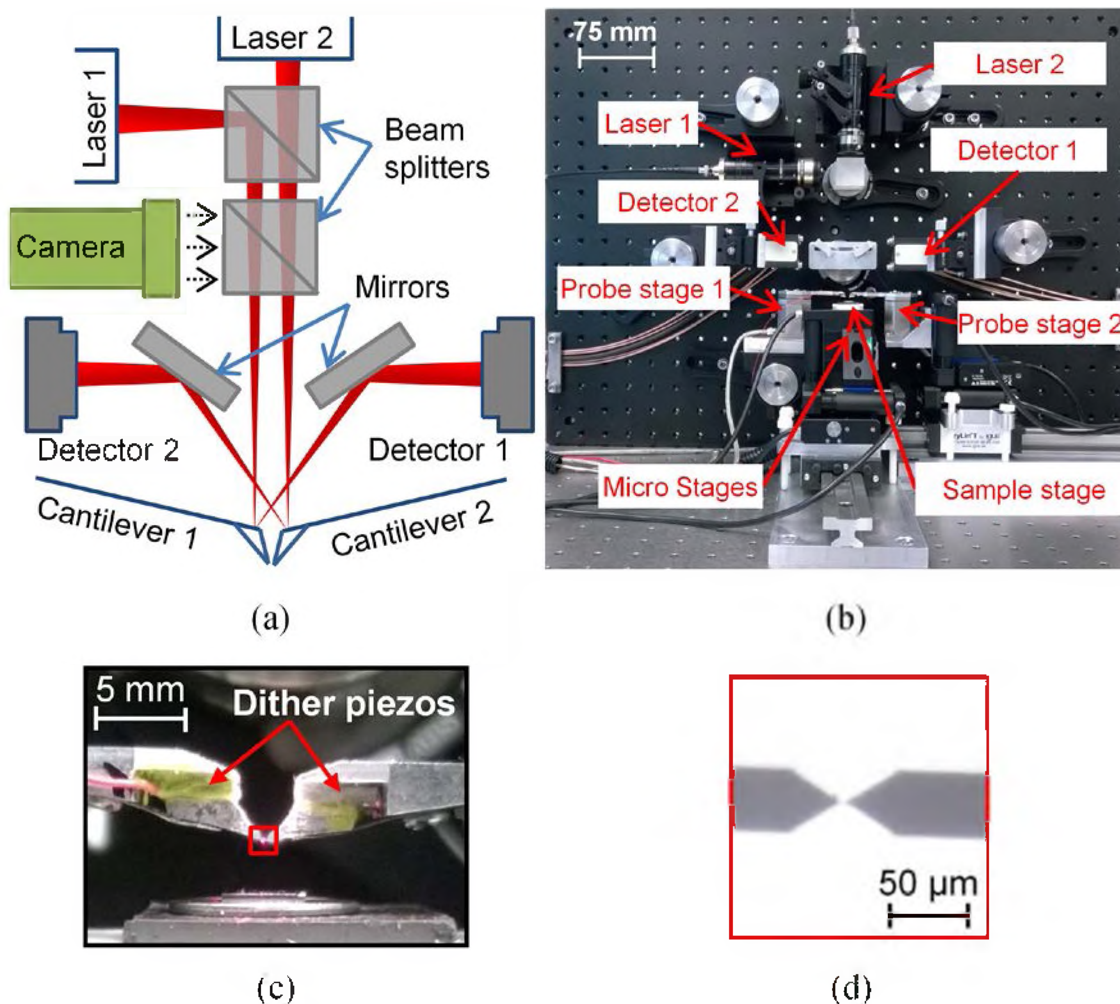

Figure 2. Schematic of dual probe arrangement (a), image of the actual DP-AFM setup (b), zoomed in image showing the probe holders with dither piezos (c), and the camera view (top view) of the two top visual probes aligned tip-to-tip (d).

Figure 2(a) shows a schematic illustrating the optical lever arrangement for both probes. The laser sources are placed perpendicular to each other, and the beams are directed towards the cantilevers using a beam splitter. The beams reflected by the cantilevers are guided to the PSD through adjustable plane mirrors. The cantilever holders are designed such that the cantilevers have a 10° pitch to reflect laser at an angle toward the PSD. A second beam splitter in the laser path serves as a window for the camera (not shown in Figure 2(b)) to monitor the probes. Figure 2(b) shows the actual DP-AFM setup. For coarse alignment, the sample nano stage and one of the probe nano stages are mounted on 3-axis micro stages (PI M112.1DG) with 25 mm range and 0.1 μm resolution. Individual components are mounted on an optical breadboard which in turn is installed on an isolation table. Using a breadboard for assembly makes the setup fully adjustable and customizable for non-standard applications. As shown in Figure 2(c), the setup also has two dither piezos (PI PIC 155) located at each probe to enable tapping mode operation when required. Figure 2(d) shows the camera view of two top visual probes (NT-MDT) aligned tip-to-tip. Though DP-AFM is capable of handling all varieties of AFM probes, these top visual probes are preferred as they place their tip leading the cantilever, which enables two probes to be aligned tip-to-tip with very minimal offset.

2.1. OPTICAL LEVER DESIGN

The optical lever is a prominent method used for detecting nanometer level displacement of the AFM cantilevers. As shown in Figure 2(a) and 3(a) a converging laser beam is focused on the back of the inclined cantilever, which gets reflected back to

a PSD. Any change in the vertical tip displacement induces a change in the slope (angular deflection, θ) at the end of the cantilever. This change in slope affects the angle of reflection of the laser beam.

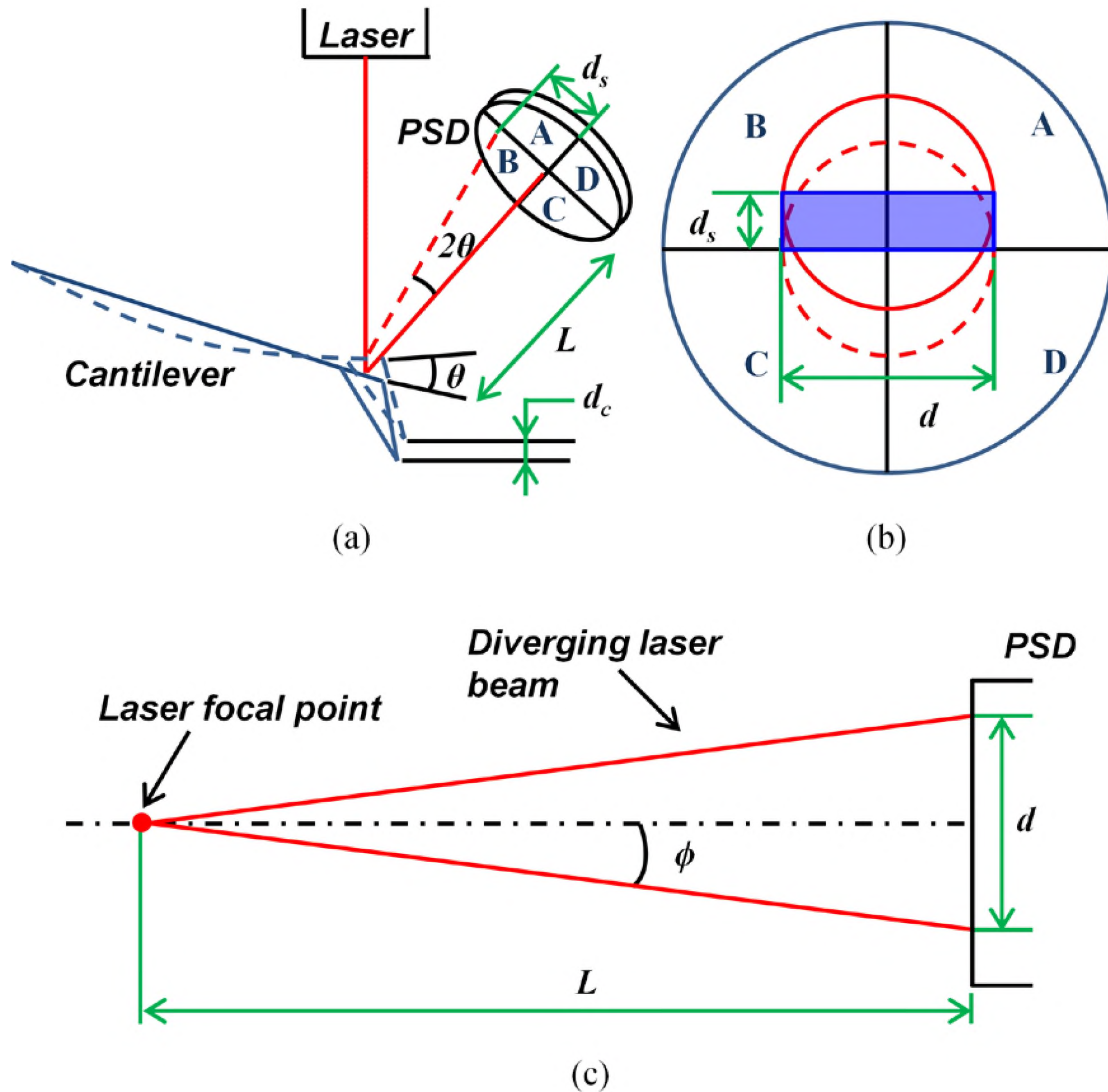

Figure 3. Schematic of a typical optical lever setup (a), laser spot displacement on the PSD which comprises of four photodetector quadrants A-D (b), schematic illustrating the cone angle of the diverging laser beam directed towards the PSD (c).

The change in the angle of reflection is captured as spot displacement (d_s) by the PSD. Consider $V_{A\text{-}D}$ as the corresponding voltage output of each quadrant A-D of the PSD. The normalized differential voltage output of the PSD is given as

$$V_{psd} = \frac{(V_A + V_B) - (V_C + V_D)}{V_A + V_B + V_C + V_D}. \tag{1}$$

Assuming the power of the laser spot on the detector is uniformly distributed across its radius, the voltage across each quadrant of the PSD can be considered proportional to the area of the segment of the spot on each quadrant. Thus, given a spot displacement d_s, the voltage sum $V_A + V_B$ is proportional to the sum of half of the spot area and the incremental spot area due to displacement d_s. Similarly, voltage sum $V_C + V_D$ is proportional to the difference of half of the spot area and the incremental spot area. On approximating the incremental spot area as a rectangle, as shown in Figure 2(a), the voltage sums can be mathematically represented as

$$\begin{aligned} V_A + V_B &\approx k\left(A_h + dd_s\right) \\ V_C + V_D &\approx k\left(A_h - dd_s\right), \end{aligned} \tag{2}$$

where, k is a proportionality constant, A_h is half of the laser spot area, d is the diameter of the laser spot. Substituting (1) in (2) and considering $A_h = \pi d^2/8$ yields

$$V_{psd} \approx \frac{dd_s}{A_h} = \frac{8}{\pi d} d_s. \tag{3}$$

One of the important design parameters in optical lever design is the optical lever sensitivity (OLS). OLS can be defined as the ratio of the change in photodetector voltage (V_{psd}) to the change in cantilever displacement (d_c),

$$OLS = \frac{V_{psd}}{d_c}. \tag{4}$$

Higher OLS implies a very small change in cantilever displacement can be detected by the PSD. Applying cantilever beam theory, the slope at the end of the cantilever can be expressed in terms of the tip displacement as

$$\theta = \frac{3}{2l} d_c, \tag{5}$$

where l is the length of the cantilever. By applying the law of reflection to the laser beam (Figure 2(a)) it can be seen that the angle of reflection of the laser beam changes by 2θ when the cantilever slope changes by θ. Moreover, from Figure 3(a) it can be observed that the spot displacement (d_s) can be written as

$$\begin{aligned} d_s &= L \tan 2\theta \\ &\approx 2L\theta \qquad (\text{for small } \theta), \end{aligned} \tag{6}$$

where L is the normal distance between the PSD and the cantilever. Substituting (5) in (6) yields

$$d_s \approx \frac{3L}{l} d_c. \tag{7}$$

Figure 3(c) illustrates the diverging laser beam reflected off the cantilever. The cantilever is usually placed at the focal point of the laser beam. The laser spot size on the PSD depends on the cone angle, ϕ, of the diverging beam and the distance between the cantilever and the PSD. Their relationship can be represented as

$$d = 2L\tan(\phi). \tag{8}$$

Substituting (26) and (8) in (3) yields

$$V_{psd} \approx \frac{12d_c}{\pi l \tan(\phi)}. \tag{9}$$

Thus, from (9), the optical lever sensitivity (OLS) can be written as

$$OLS = \frac{V_{psd}}{d_c} \approx \frac{12}{\pi l \tan(\phi)}. \tag{10}$$

While the cantilever length, l, is often fixed, the optical lever sensitivity can be increased by decreasing the cone angle of the laser beam. This is achieved by using a laser shutter at the source that radially cuts the laser beam. The cone angle in our setup is 0.65°. Hence, for a cantilever of length 450 μm, the OLS theoretically calculated using (10) is 0.75 mV/nm. Experimentally, OLS was calculated by performing the approach-retract experiment [23-24]. The approach-retract experiment involves moving the probe towards and away from a hard sample, and monitoring the PSD voltage. The PSD voltage is plotted against the sample stage displacement, and the slope of the curve provides the experimental OLS. Figure 4 shows the results of the experimental approach-retract curve, and the slope of the curve is 0.80 mV/nm. Considering (10) being a theoretical

approximation for OLS and ±20 μm (supplier specification) uncertainty in the cantilever's length, the experimental OLS is in good agreement with the theoretical value.

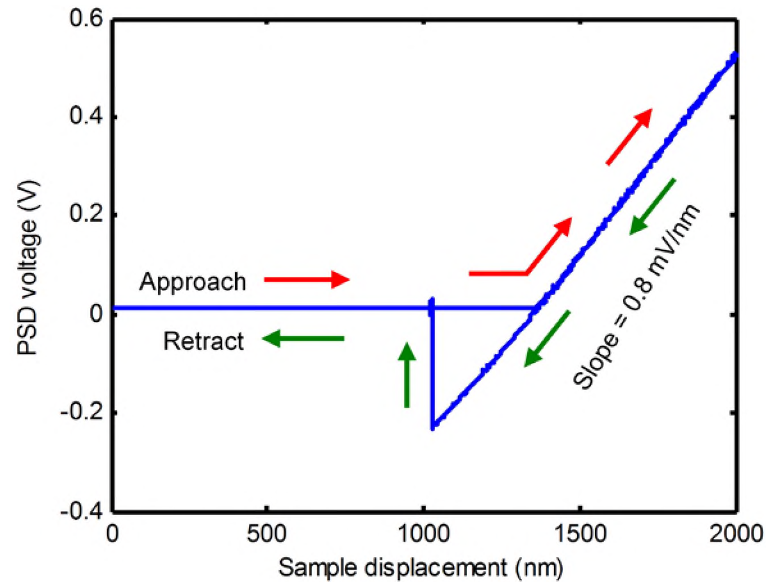

Figure 4. Experimental PSD voltage vs. sample stage displacement (Approach-retract curve). The slope of the linear segment is 0.8 mV/nm, which is the experimental OLS.

2.2. CONTROLLER AND SOFTWARE DESIGN

The instrument control functionality is divided between two processors. A standard Windows PC provides high-level control including user interface, process planning, and image processing. A National Instruments PXI real-time system (NI PXIe-8135) provides low-level control such as individual feedback loops for stage control, scanning and trajectory generation, alignment routines etc. Figure 5 shows the control system layout of the DP-AFM. A loop rate of 10 kHz was chosen for the real-time system based on the trade-off between high bandwidth requirements and computation overhead.

Analog I/O boards (NI PXI-6733 and NI PXIe-6368) handle signals to and from the stages.

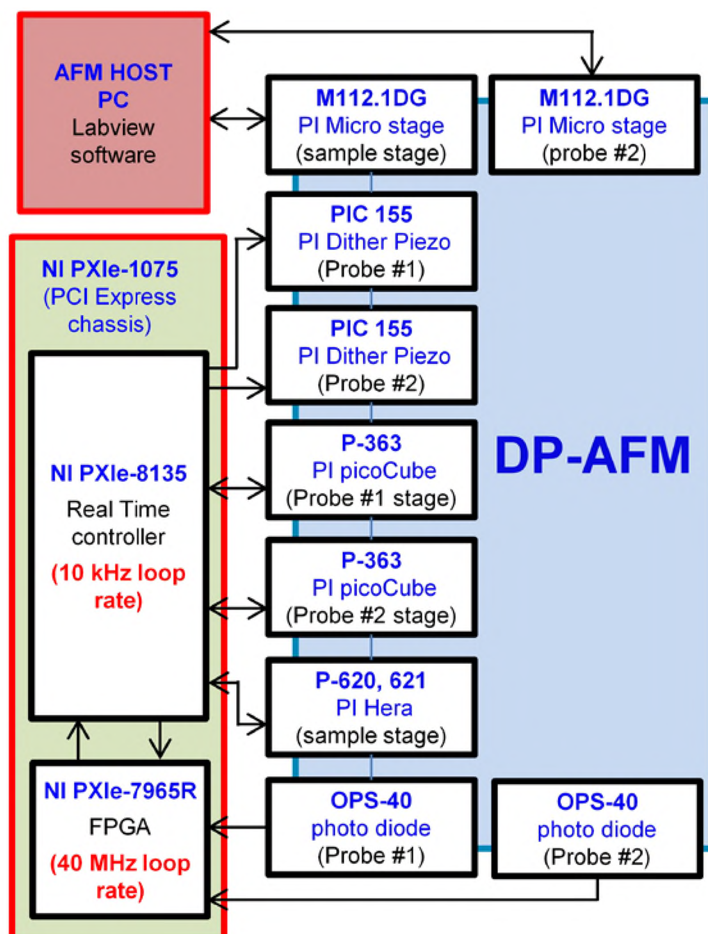

Figure 5. Instrument control layout showing the interconnections of various components of the DP-AFM.

High-speed signals, like tapping mode oscillation signals which are ~300 kHz, are handled using field-programmable gate array (NI PXIe-7965R). FPGA provides high speed (40 MHz loop rate) signal processing and computation capabilities. The real time and non-real time processes are programmed using Labview software. Figure 6 shows the software components involved in operating a single probe. The layout is identical for the

other probe and hence is not shown in Figure 6. The cantilever can be operated in either tapping mode or contact mode. Regardless, the PSD signal is acquired by the FPGA at 40 MHz sampling rate. In tapping mode, the PSD signal is often a sinusoidal signal corresponding to the tip amplitude.

In contact mode, this signal represents the deflection of the cantilever. Usually, in tapping mode, the RMS of the tip oscillation is regulated, while in contact mode the cantilever deflection is regulated, to generate an image of the surface topography. The FPGA calculates the RMS of the signal by low-pass filtering the square of the PSD signal and then performing square root operation on the filtered output. Figure 6(b) shows a block diagram illustrating different operations in the RMS filter. The cut-off frequency of the low-pass filter was chosen to be 5 kHz so that the filter will also act as an anti-aliasing filter, thus preventing aliasing when the signal is transferred to the real-time loop running at 10 kHz. When operating in contact mode the PSD signal is directly filtered using an anti-aliasing filter and communicated to the real-time loop. Based on the mode, the corresponding FPGA signal is chosen in the real-time loop and is regulated by controlling the Z-axis of the probe stage. The XY axes perform raster scan to generate the sample topography. Alternatively, the sample stage can be used for imaging and raster scanning based on the range requirements.

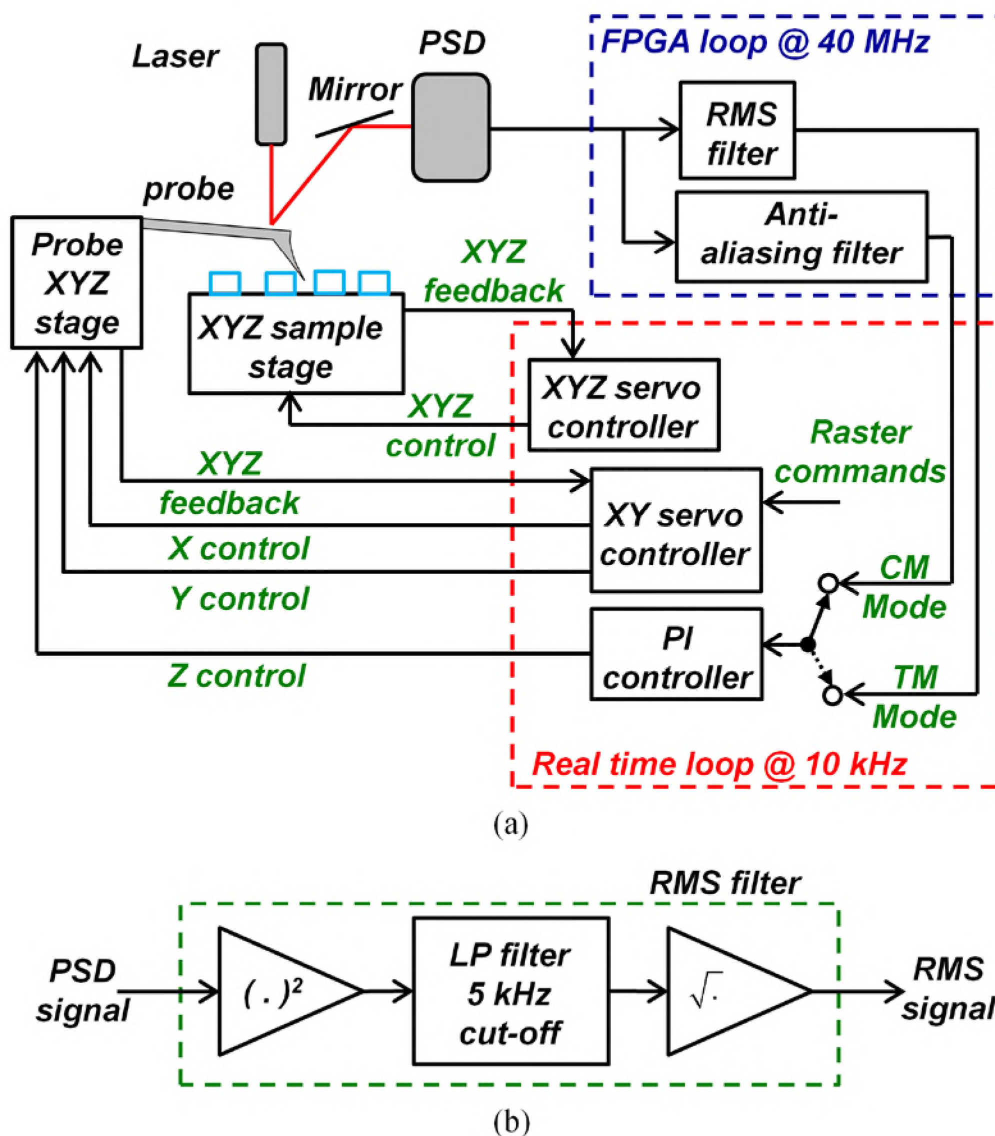

Figure 6. Schematic of (a) software components involved in operating a single probe for imaging. The other probe involves identical components for its operation, and hence is not shown. Block diagram representation of a RMS filter is shown in (b).

3. DP-AFM CALIBRATION PROCEDURES

Unlike single probe AFM which often has a stationary probe, DP-AFM has probes installed on precision nano stages. Movable probe setup poses two key challenges. First, with a stationary laser source aligned to focus the beam on the probe, any change in

probe position would misalign the laser, which would affect the deflection measurement. Second, manually aligning both the probes tip-to-tip within certain microns offset, with limited visual feedback from the camera, is challenging, and requires an automated procedure. These issues and their proposed solutions are discussed in the following sections.

3.1. 3D PROBE POSITION ERROR COMPENSATION

The tip deflection in an AFM is measured by measuring the laser spot displacement on the PSD caused by the change in slope at the end of the probe. However, the change in probe position also displaces the spot on the PSD. This spot displacement changes the PSD output voltage, which could be misinterpreted as tip deflection. This phenomenon is illustrated in Figure 7. Hence, it is important to decouple the effect of probe position on the deflection measurement. This is achieved by constructing an error model that best captures the change in voltage as a function of the probe position and compensating for it. Mathematically, the compensated PSD voltage V_{comp}, at any time t, can be represented as,

$$V_{comp} = V_{uncomp} - e(x, y, z), \tag{11}$$

where, V_{uncomp} is the uncompensated PSD voltage measurement affected by probe position changes, (x, y, z) is the position of the probe stage, and $e(x,y,z)$ is the 3D error model of voltage change due to probe position. The error model, $e(x,y,z)$, is constructed by calculating the voltage error at discrete coordinates (x_i,y_i,z_i) and fitting a 2nd order 3D polynomial using least square fit.

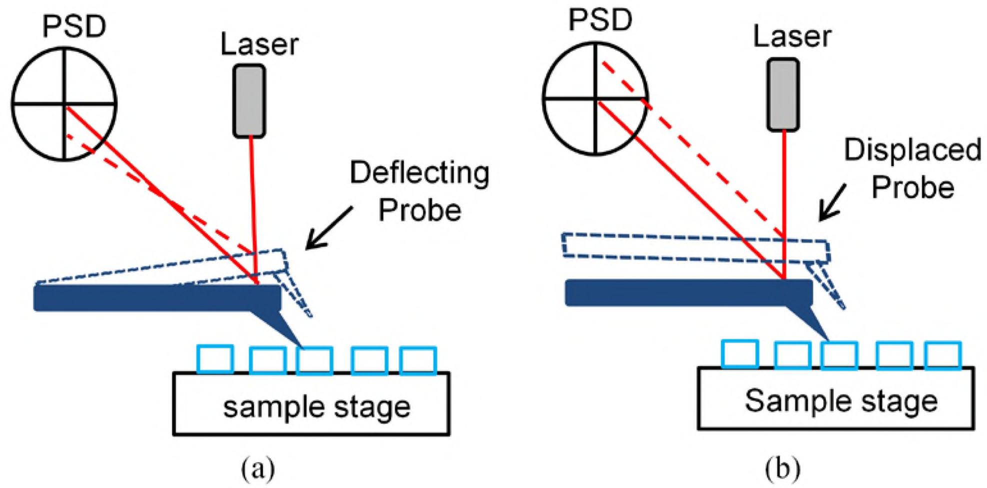

Figure 7. Illustration of (a) laser spot displacement on the PSD due to tip deflection, and (b) spot displacement due to change in probe position which could be misinterpreted as tip deflection.

The measured voltage error $e_i(x_i,y_i,z_i)$ is given by

$$e_i(x_i, y_i, z_i) = V(x_i, y_i, z_i) - V_0, \tag{12}$$

where, $V(x_i,y_i,z_i)$ is the voltage measured at the coordinate (x_i,y_i,z_i), i=1,2,...n and V_0 is the voltage measured at the nominal position of the probe stage which corresponds to the true alignment of the laser. The general 2nd order 3D polynomial describing the error model can be represented as

$$\begin{aligned} e(x,y,z) = {} & a_1x^2 + a_2x + a_3y^2 + a_4y + a_5z^2 + a_6z \\ & + a_7xy + a_8xz + a_9yz + a_{10}. \end{aligned} \tag{13}$$

Given the set of discrete voltage error measurements as described in (12), the best fit polynomial can be obtained by solving the set of equations that can be written in matrix form as

$$PA = E, \tag{14}$$

where,

$$P = \begin{bmatrix} x_1^2 & x_1 & y_1^2 & y_1 & \dots & 1 \\ x_2^2 & x_2 & y_2^2 & y_2 & \dots & 1 \\ . & . & . & . & . & . \\ . & . & . & . & . & . \\ x_i^2 & x_i & y_i^2 & y_i & \dots & 1 \end{bmatrix}, E = \begin{bmatrix} e_1(x_1, y_1, z_1) \\ e_2(x_2, y_2, z_2) \\ . \\ . \\ e_i(x_i, y_i, z_i) \end{bmatrix},$$

and $A = [a_1 \quad a_2 \quad \dots \quad a_{10}]^T$.

The least square solution [25] of (14) is given as

$$A = P^+ E, \tag{15}$$

where $P^+ = (P^T P)^{-1} P^T$ is the pseudo inverse of the matrix P. The vector A, calculated using (15), provides the coefficients of the polynomial error model denoted in (13). In order to validate the compensation algorithm, an experiment was conducted in which the probe stage was moved to 1000 quasi-random coordinates (Figure 8(a)) over their full range (0 to 5 μm), while the probe was in the undeflected state, and the compensated and uncompensated PSD voltage were measured. Ideally, without any probe deflection, the PSD voltage should be zero, but due to the random probe stage motion the PSD falsely detects deflection around 25 nm peak-to-peak. However, post-compensation the deflection is around 0.58 nm peak-to-peak, which is approximately two orders of magnitude smaller than the uncompensated deflection measurement.

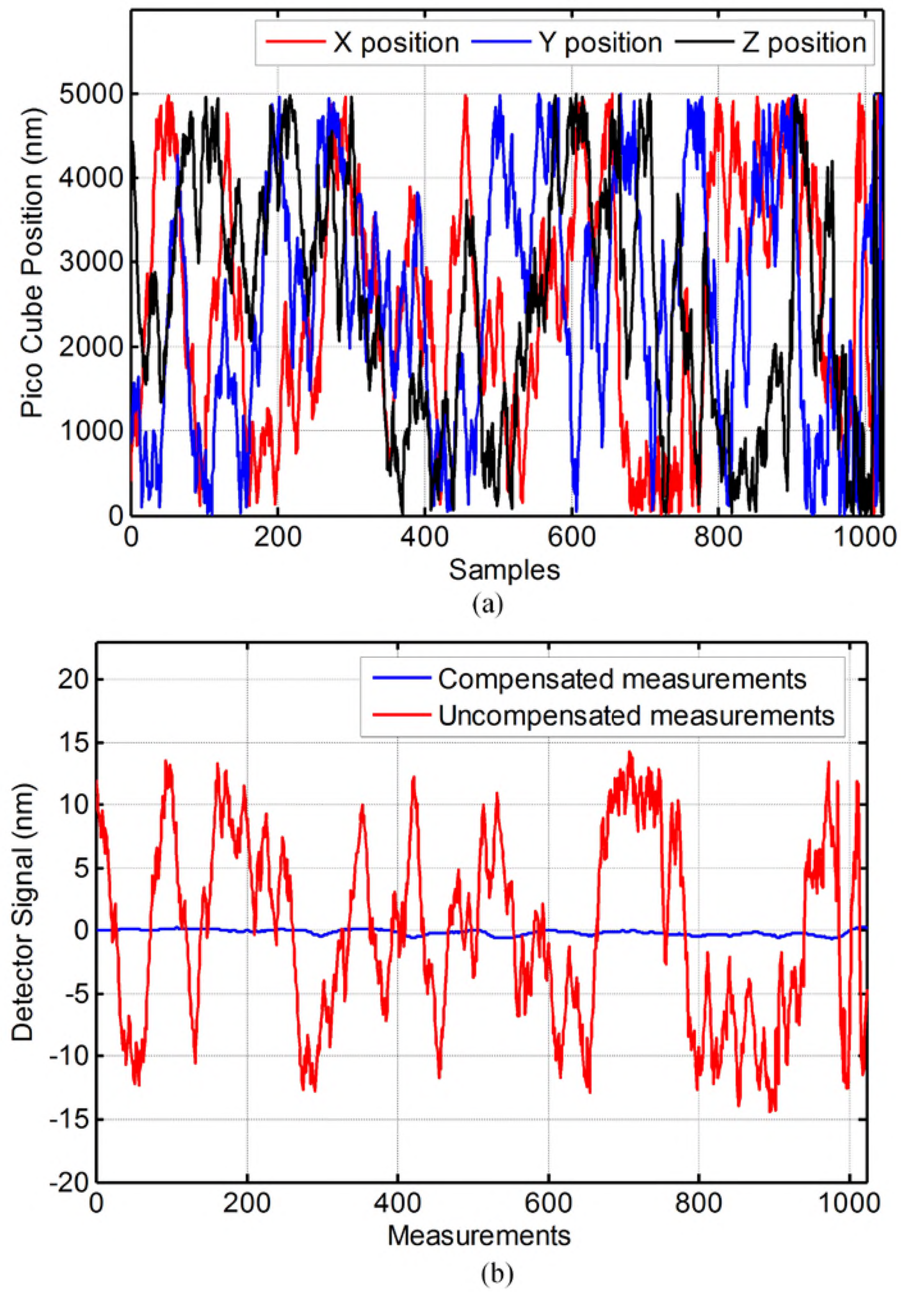

Figure 8. Plots showing (a) Quasi-random motion of the individual probe axes, and (b) Comparison between compensated and uncompensated deflection signal when the probe stages are traversed in a quasi-random trajectory.

3.2. DUAL-PROBE ALIGNMENT PROCEDURE

As mentioned in section 2, the probes are installed on two 3-axis nano stages. In addition, probe 2 is installed on a 3-axis micro stage to enable coarse alignment of the probes. For some dual-probe applications the tip-to-tip alignment, with certain known offset between them is necessary. Locating the probes is achieved through direct physical contact with each other. However, searching for the probe tip, with another probe tip, in 3D space is challenging. Though it is possible to align them within sub-millimeter accuracy with the help of the visual feedback from the camera, finer alignment requires a more systematic procedure. A three-step process is used here and is illustrated in Figure 9. First, the probes are coarsely aligned in all the three directions with help of the camera. Second, the probes are aligned along the z-axis by sequentially engaging both the probes to the sample, followed by withdrawing the sample. Engaging here refers to approaching the sample with the probe until a desired deflection (contact mode) or RMS amplitude (tapping mode) is achieved. If the sample is relatively flat with sub-micron features, the probes will also be aligned in the z-axis within sub-micron accuracy. This results in the tips being approximately located in the same XY plane. Third, probe 2 is made to search for probe 1 in a raster pattern along the XY plane. The search pattern involves a fine raster search by the probe stage followed by a translation along X and Y axis by the micro stage as shown in Figure 9(d), thus executing a 2D grid search. The micro stage by itself follows a crude raster pattern by moving the probe to adjacent grids as numbered in Figure 9(d). This procedure is carried out until probe contact is detected. Once the contact is made, probe 2 can be moved with reference to probe 1 to maintain a known tip offset.

Detecting contact between the probes is crucial for their alignment. It can be observed from the 2D raster search pattern described above, when the probes are brought close to each other, the first contact occurs between the side faces of the tip. Such an interaction induces a torsional force along the longitudinal axis of both the probes. This results in the probes twisting along their respective longitudinal axes. Such twisting can be measured using the horizontal channel of the PSD, which can be used to detect probe contact.

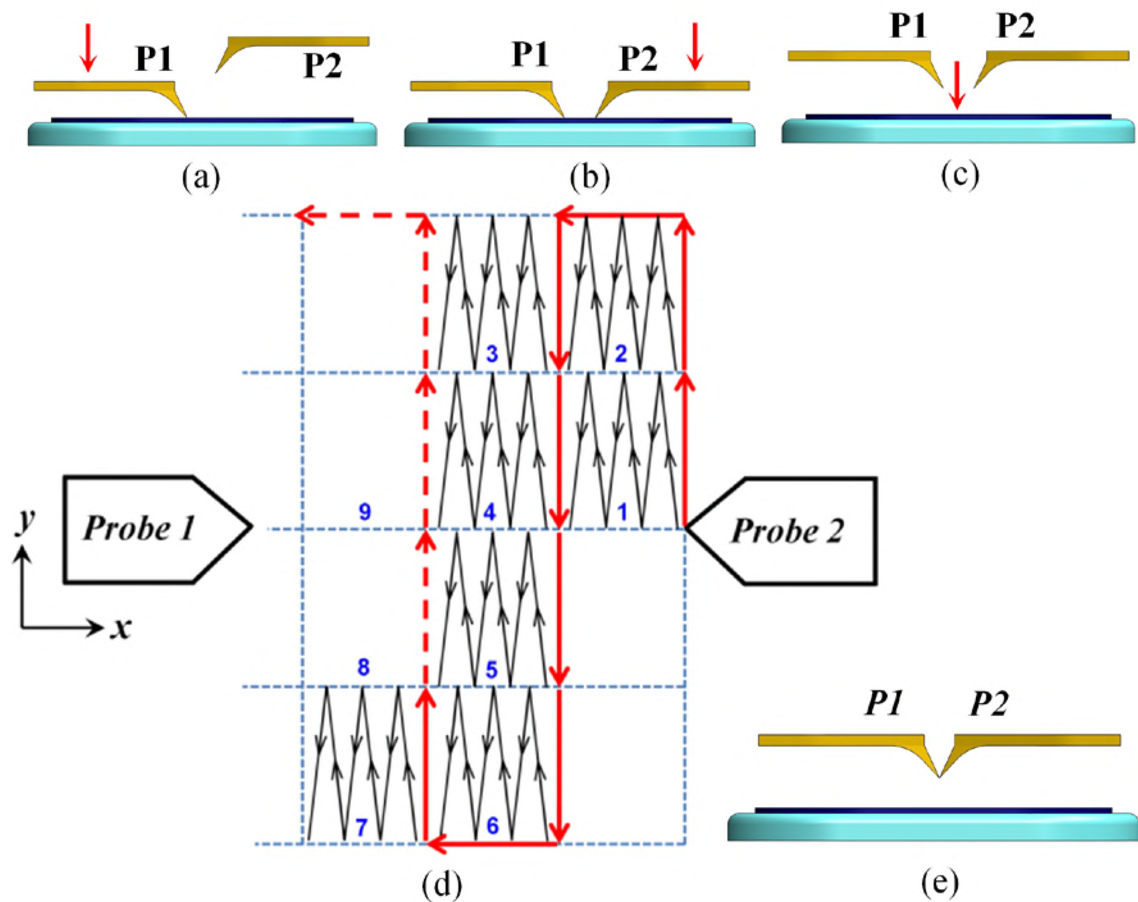

Figure 9. Steps involved in aligning the probes in 3D space. (a) Probe 1 is engaged to the sample. (b) Probe 2 is engaged to the sample. (c) Sample is withdrawn leaving the probes approximately in the same XY plane. (d) 2D raster search pattern traversed by the moving probe. (e) Two probes in contact with each other.

Figure 10 shows the horizontal channel signal of both the PSD when a contact mode probe (nominal stiffness 0.53 N/m) was made to search for a non-oscillating tapping mode probe (nominal stiffness 60 N/m). As long as there is no contact the channels read zero voltage. When contact occurs, the probes twist in opposite directions. This can be observed in the Figure 10 where the signals have opposite phase after contact. Since contact mode probe is less stiff than tapping mode, its horizontal signal is larger compared to contact mode. Once the contact probe moves past the tapping mode probe both the probes return to their equilibrium position.

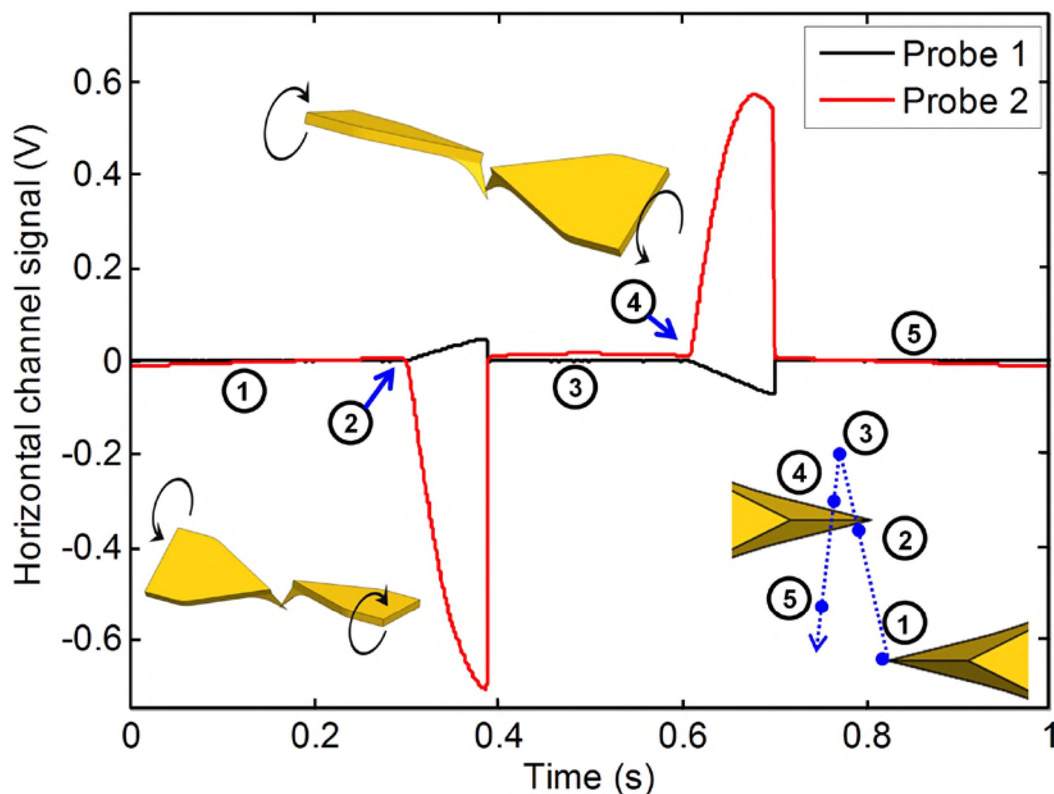

Figure 10. The horizontal channel signal of a contact and tapping-mode probes when contact mode probe was used to raster search the tapping-mode probe. The inset shows the different stages of contact while searching for the probe.

A similar trend is observed when the contact probe approached the tapping mode probe from the other direction. Thus probe contact can be detected by checking when the horizontal signals cross a certain threshold.

4. CLOSED-LOOP PLOWING

One of the fundamental nanoscale material removal processes that can be performed using an AFM is plowing [26-27]. Plowing is performed by using the AFM tip to apply a mechanical force normal to the surface while the tip is in motion such that the substrate undergoes plastic deformation. Typically, the tip or the substrate is mounted on a 3-axis positioner, and the required force is applied by pressing the tip and the substrate against each other. This is followed by moving the positioner along a prescribed path to obtain a desired plow profile. Because a single-probe AFM cannot simultaneously plow and image, the plowing process occurs first in open-loop followed by imaging the profile to assess the plow depth. Based on the results, the process parameters are calibrated iteratively through trial-and-error, until the plow profile has the desired depth. This trial-and-error method is cumbersome, and often the presence of process uncertainties (probe stiffness, tip wear) affects the quality of the plowed profile. The problem of obtaining a desired plow depth, irrespective of process uncertainties, can be effectively addressed by monitoring and controlling the plowing process in real time using the DP-AFM. In this application, one probe can be made to plow the substrate while the other probe can be used to image the plow profile, and in the process provide a feedback on the actual plow depth. With the depth feedback available, a real-time process control scheme can be

designed to regulate the plow depth. The mathematical model of the plowing process and the process control design are discussed in the following sub-sections.

4.1. PLOWING MODEL DESCRIPTION

The dynamics of the plowing probe interaction with the substrate can be best captured by modeling it as a spring-mass-damper system [28],

$$m\ddot{\delta}(t)+c\dot{\delta}(t)+\left(k_{pr}+k_s\right)\delta(t)=c\dot{u}(t)+k_{pr}u(t), \tag{16}$$

where δ is the displacement of the tip from its equilibrium position, u is the probe base position, k_s is the substrate stiffness, and m, c, k_{pr} are equivalent mass, damping coefficient, and stiffness of the probe respectively. Figure 11(a) shows a schematic of the plowing operation and Figure 11(b) shows the spring-mass-damper representation of the plowing probe interaction with the substrate.

The substrate is assumed to be fixed and the plowing probe is assumed to be mounted on a 3-axis positioner. Thus the plowing force can be exerted by applying the cantilever base motion, u in the downward direction. The plow depth, d can be expressed as a function of tip displacement as

$$d(t)=\begin{cases}\delta(t) & \delta>0\\ 0 & \delta<0\end{cases}. \tag{17}$$

In practice, the cantilever properties and the substrate stiffness are uncertain parameters, and from (16) it is clear they affect the plow depth. Thus it is challenging to obtain plow profile with a desired depth, and the often cumbersome trial-and-error procedure is

followed to get the required plow profile. Moreover, as the plow profile becomes more complex, the trial-and-error procedure becomes tedious. This highlights the importance of feedback control of plowing process where the plow depth can be made to robust to process uncertainties like the cantilever and substrate stiffness.

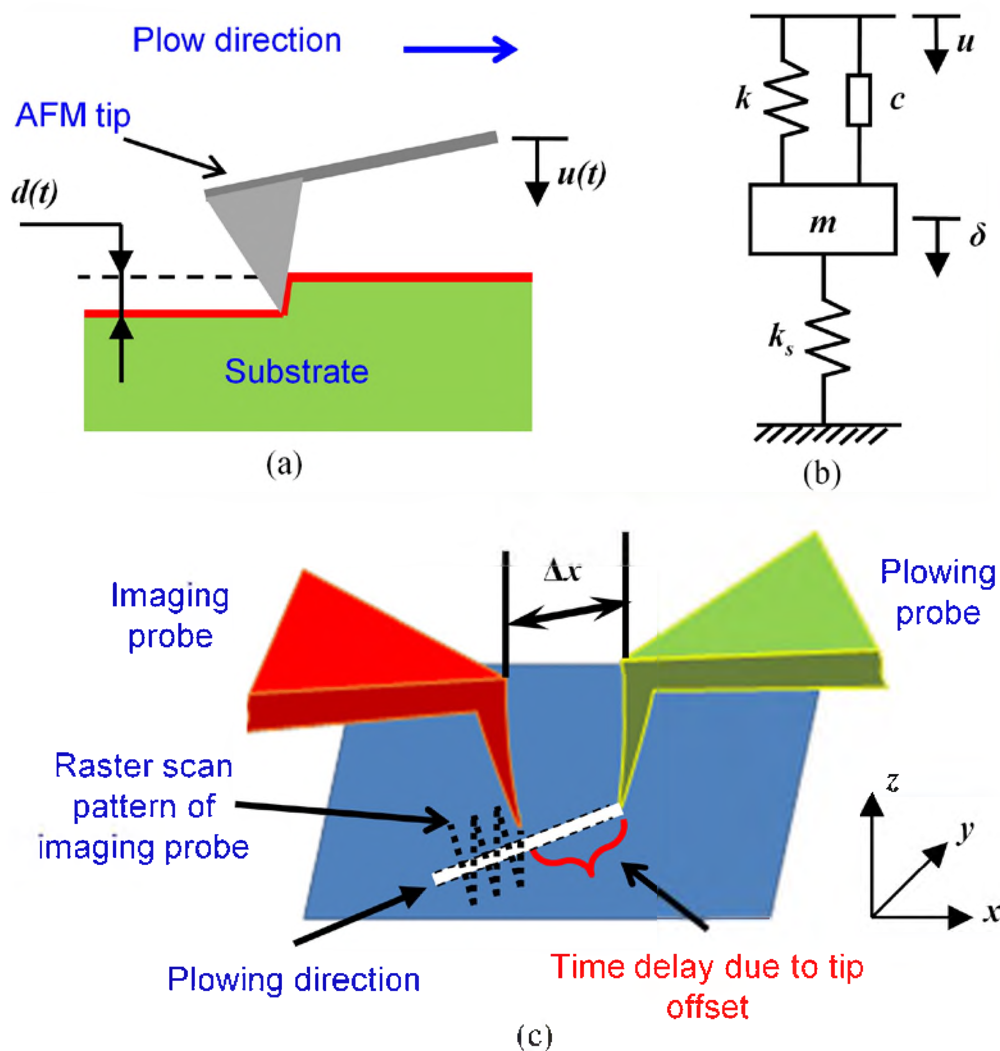

Figure 11. Schematic of the plowing process (a), Spring-mass-damper representation of the probe-substrate interaction (b), and tip-to-tip probe setup in DP-AFM for plowing process control (c). The imaging probe trails the plowing probe by a spatial offset of Δx, which induces a time delay in the plow depth measured by the imaging probe.

The DP-AFM plowing process control is illustrated in Figure 11(c). As the plowing probe performs its operation, the imaging probe follows the plowing probe along the plowing direction, while raster scanning the plowed profile. Though DP-AFM is capable of providing real-time plowing measurements, to avoid collisions, a small offset, Δx is maintained between the tips. This introduces a time delay in the measurement made by the imaging probe. The delayed measurement can be represented as

$$d_d(t) = d(t-\tau),\ where\ \tau = \Delta x / v_p, \tag{18}$$

where $d_d(t)$ is the plow depth measured by the imaging probe at time t and v_p is the probe velocity along the plow direction. The time delay in the measurement poses a control challenge, but the fact that Δx is usually known, and v_p is a process parameter that can be suitably set makes τ a known parameter. Next section discusses the control design that enables plowing process control even in the presence of measurement time delay.

4.2. CONTROL FORMULATION

The real time measurement of the plow depth, albeit with a certain time delay, enables the implementation of a feedback controller that can regulate it to a desired value, irrespective of process uncertainties. Plow depth measurement is carried out by raster scanning across the plowed profile. Since the scan speed of a typical AFM is 1-10 Hz, the sampling rate of the feedback signal is limited by the scan speed. Given that the feedback signal has a maximum sampling rate of 10 Hz, the controller’s sampling rate is chosen to be 100 Hz which is orders of magnitude slower compared to the AFM cantilever

dynamics (natural frequency >1 kHz). Thus the model presented in (16) is simplified to a static model by considering the steady-state solution of (16), which is

$$G = \frac{d(t)}{u(t)} = \frac{k_{pr}}{\left(k_{pr} + k_s\right)}, \qquad \delta(t) > 0. \tag{19}$$

Given a static process with time delay in the feedback, a proportional-integral (PI) controller augmented with a Smith predictor [29-30] is used to track the desired plow depth. While PI controller provides a straightforward solution for the tracking problem, the smith predictor makes the process robust to time delay of known magnitude. The PI controller is described as

$$u(t) = k_p e(t) + k_i \int_0^t t(\tau)\, d\tau, \tag{20}$$

where k_p and k_i are the proportional and integral gains. The tracking error is defined as

$$e(t) = d_r(t) - d(t), \tag{21}$$

where $d_r(t)$ represents the desired plow depth to be tracked. The gain values are tuned based on the desired transient and steady state performance. The Smith predictor structure for the plowing control can be written as

$$C_{sp}(s) = \frac{E_1(s)}{U(s)} = \hat{G}\left(1 - e^{-\tau s}\right), \tag{22}$$

where $\hat{G}$ is the model of the actual process gain G. E_1(s) and $U(s)$ are the Laplace transform of signal $e_1(t)$ and tip base position $u(t)$. The measurement time delay τ can be

held constant by maintaining a constant tip offset Δx and plow velocity v_p, as indicated in (18). A block diagram illustrating the closed loop plowing process is shown in Figure 12. The controller and Smith predictor presented in (20) and (22) are discretized with time step 0.01 seconds (sampling rate 100 Hz) for software implementation. The imaging probe scans across the plow profile every T_{im} seconds which is the inverse of the raster scan rate. The measured scan line is processed in real time to calculate the plow depth. This calculated value serves as a feedback to the controller. In order to match the controller sampling rate, the plow depth signal is upscaled using zero-order hold.

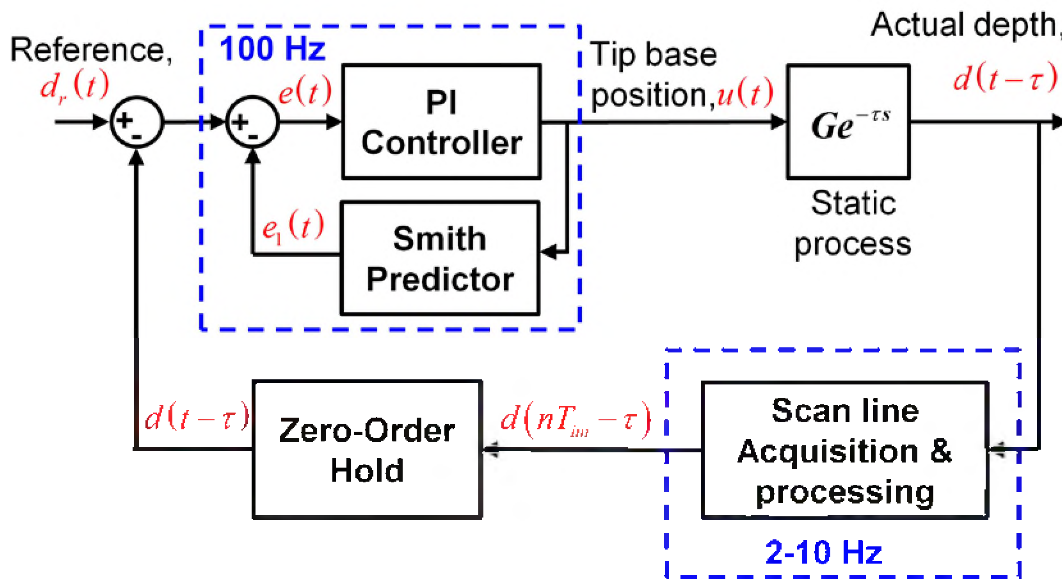

Figure 12. Block diagram representation of the plowing process control. The continuous plowing process is measured at discrete time intervals of size T_{im} which correspond to the scan rate of the imaging probe. The scan line data arrives at rate of 1-10 Hz and is upscaled using zero-order hold method to match the controller execution rate of 100 Hz.

The plow depth calculation is itself carried out in two steps. First, typically AFM scan line data has a slope associated with it, because AFM tips are often not loaded

normal to the sample it is scanning. This slope is removed by subtracting the best line fit from the data. Figure 13(a) shows a typical scan line data of the plowed profile and the best line fit. Second, the plow depth is calculated using the flattened scan line as

$$d = \mathrm{Avg}(A, B) - \min(S), \tag{23}$$

where, A and B, as illustrated in Figure 13(b), are the first n and last n data points of the flattened scan line data array S.

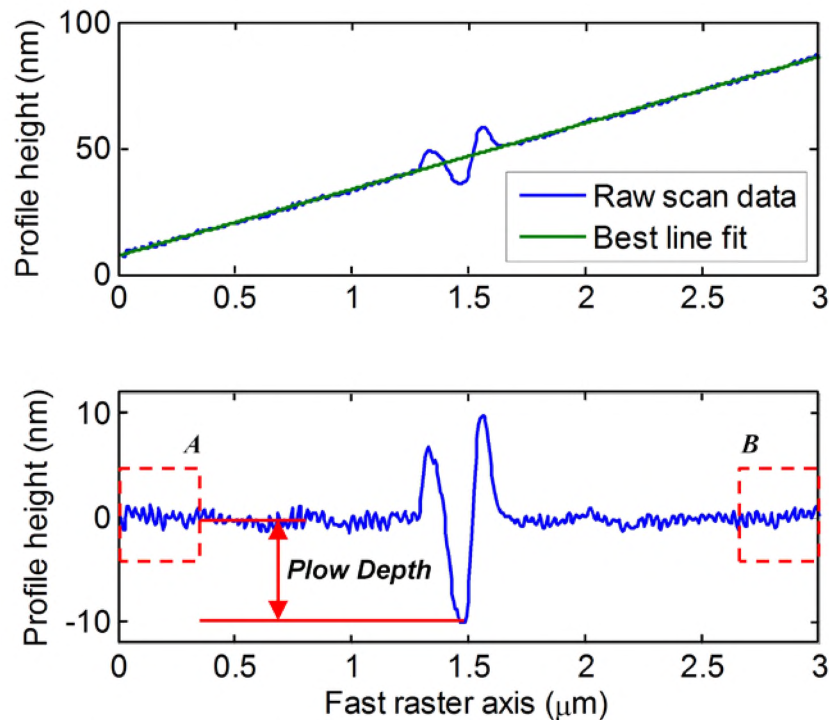

Figure 13. Plots showing (a) raw scan line data of the plow section generated by the imaging probe and the best line fit of the data, and (b) flattened scan line obtained by subtracting the best line fit from the raw data.

The assumption behind calculating plow depth using (23) is that the substrate is relatively flat and the plowed section is approximately at the center of the scan. In Figure 13(b), the

size of the windows A and B are chosen heuristically to be 50, but it can be varied as long as the windows avoid the plow section.

5. EXPERIMENTAL RESULTS & DISCUSSION

To provide a baseline performance, first, a series of lines were plowed with constant process parameters, in open-loop with a visual top probe (NT-MDT VIT_P silicon probes). A 2 μm thin polymer film (SU-8 photoresist polymer) was chosen as the plowing substrate. The experiment involved plowing four parallel lines at different locations on the substrate. Figure 14 shows the 2D images of plowed lines and their plow section.

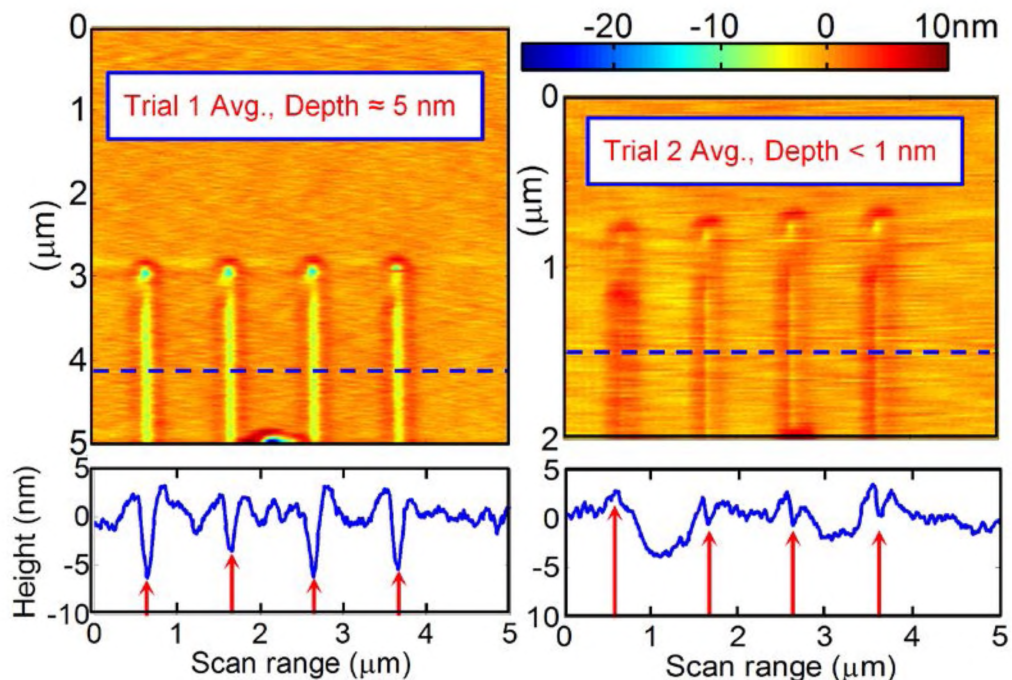

Figure 14. 2D images of two sets 4 parallel lines plowed in different locations on the same substrate. The section images show the variation in the plow depth due to the presence of process uncertainties.

It can be observed that the same process settings yield varying plow depth. This is due to the presence of process uncertainties such as varying substrate stiffness (different locations tend to have different stiffness) and tip wear.

The closed-loop experiment involved plowing a straight line on the polymer substrate while having the imaging probe measure the plow profile in real-time. The controller shown in Figure 12 was implemented using Labview software. Two visual top tapping mode AFM probes were aligned tip-to-tip with a tip offset (Δx) of 2 μm. The plowing velocity, v_p was set to 1 μm/s, thus resulting in an effective time delay ($\hat{\tau}$) of 2 seconds. The process gain estimate, $\hat{G}$, was set to 0.025. The process control gains were set as follows: k_p=4, and k_i=40. Plowing was performed by moving the sample stage along the plowing axis, such that the imaging probe measures the part that is already plowed. The imaging probe was made to raster scan across the plowed profile at a scanning rate of 4 Hz. Figure 15(a) shows the 2D image of the plow profile when a step change from 10 nm to 25 nm was set as the reference depth. Initially, the plowing tip is not in contact with the surface. However, the controller asymptotically converged the actual depth to the desired value. The step change in the plow depth can be clearly observed from the 2D image. Figure 15(a) also shows the real-time plow depth measured by the imaging probe with respect to the plowing probe position. Though the plowed line was 20 μm long, the feedback from the imaging probe was only available up to 18 μm, as there is a 2 μm offset between the probes. Figure 15(b) shows the section of the steady-state plow profile before and after the step change. It is important to note that this process did not involve any extensive calibration of the probe or experiments to determine the sample stiffness. Irrespective of these uncertainties the controller provided asymptotic

convergence. Additionally, though there is a delay in the measurement, the controller was able to mitigate its effect on the tracking performance.

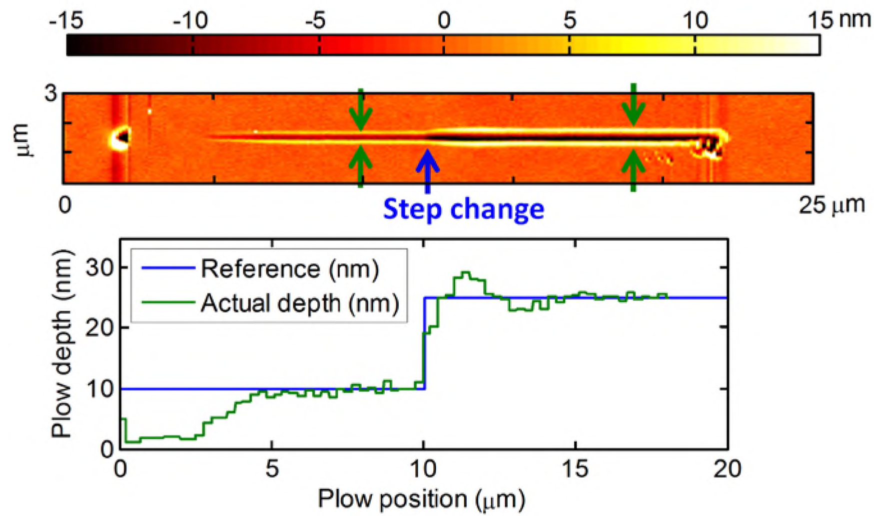

(a)

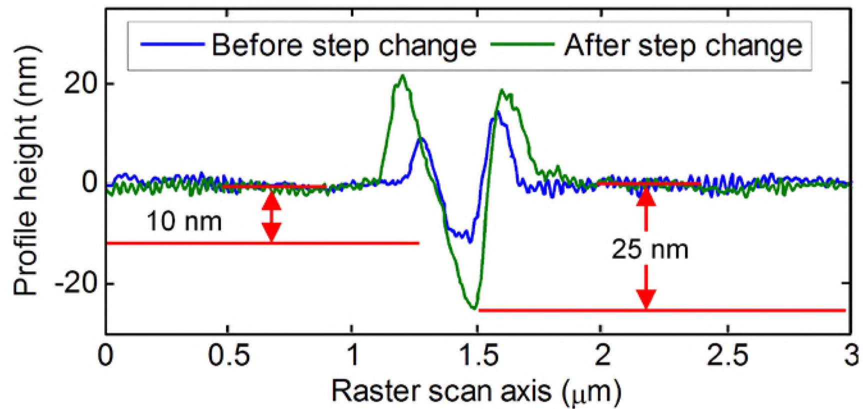

(b)

Figure 15. 2D image of the plowed profile with a step change in depth of cut from 10 to 25 nm, and the plow depth with respect to the plow probe position are shown in (a). The scan line data of the plowed line at the location marked by the green arrows in Figure 15(a) is plotted in (b).

6. CONCLUSIONS

A major limitation in single-probe AFM for nanofabrication is that the process cannot be monitored. This is because the AFM probe cannot simultaneously image while in fabrication mode. Alternating between imaging and fabrication mode is often cumbersome and challenging. Toward the automation of AFM nanomanufacturing, we have developed a dual-probe AFM which has two independent probes operating in a common workspace. While one probe can be used to carry out one of the many nanofabrication tasks, the other probe can monitor the task. This provides real-time feedback, which in turn provides a basis for automation. This functionality of the DP-AFM was demonstrated here in the nanoscale plowing process. Two independent probes in DP-AFM are used to plow and measure the plowed depth simultaneously. This enables the formulation of closed-loop control to regulate the plow depth. The measurement time delay due to the spatial gap between the probes is effectively addressed by augmenting the PI controller with a smith predictor. The effectiveness of the controller was verified experimentally by plowing a straight line on a polymer substrate. The results indicate that the desired plow can be varied on the fly, enabling the user to plow complex cutting profiles with limited user intervention, all the while maintaining nanometer-level accuracy.

REFERENCES

[1] G. Binnig and C. F. Quate, "Atomic Force Microscope," *Physical Review Letters*, 56(9), pp. 930-933, 1986.

[2] R. Garcia and R. Perez, "Dynamic atomic force microscopy methods," *Surface Science Reports*, 47, pp. 197-301, 2002.

[3] N. Jalili and K. Laxminarayana, "A review of atomic force microscopy imaging systems: application to molecular metrology and biological sciences," *Mechatronics*, 14, pp. 907-945, 2004.

[4] C. A. Putman, K. O. Van der Werf, B. G. De Grooth, N. F. Van Hulst, and J. Greve, "Tapping mode atomic force microscopy in liquid," *Applied Physics Letters*, 64(18), pp. 2454-2456, 1994.

[5] S. I. Kitamura, and M. Iwatsuki, "High-resolution imaging of contact potential difference with ultrahigh vacuum noncontact atomic force microscope," *Applied Physics Letters*, 72(24), pp. 3154-3156, 1998.

[6] T. Nitta, H. Haga, K. Kawabata, K. Abe, and T. Sambongi, "Comparing microscopic with macroscopic elastic properties of polymer gel," *Ultramicroscopy*, 82(1), pp. 223-226, 2000.

[7] S. J. T. Van Noort, O. H. Willemsen, K. O. van der Werf, B. G. de Grooth, and J. Greve, "Mapping electrostatic forces using higher harmonics tapping mode atomic force microscopy in liquid," *Langmuir*, 15(21), pp. 7101-7107, 1999.

[8] J. J. Saenz, N. Garcia, P. Grütter, E. Meyer, H. Heinzelmann, R. Wiesendanger, L. Rosenthaler, H. R. Hidber, and H. J. Güntherodt, "Observation of magnetic forces by the atomic force microscope," *Journal of Applied Physics*, 62(10), pp. 4293-4295, 1987.

[9] M. Sitti, "Survey of nanomanipulation systems," in *Proc. IEEE-NANO*, pp. 75-80, 2001.

[10] G. Li, N. Xi, H. Chen, A. Saeed, and M. Yu, "Assembly of nanostructure using AFM based nanomanipulation system," *IEEE International Conference on Robotics and Automation (ICRA)*, pp. 428-433, 2004.

[11] G. Li, N. Xi, H. Chen, C. Pomeroy, and M. Prokos, "Videolized atomic force microscopy for interactive nanomanipulation and nanoassembly," *IEEE Transactions on Nanotechnology*, 4(5), pp.605-615, 2005.

[12] R. D. Piner, J. Zhu, F. Xu, S. Hong, and C. A. Mirkin, “"Dip-pen" nanolithography”. *Science*, 283(5402), pp. 661-663, 1999.

[13] R. W. Carpick, and M. Salmeron, “Scratching the surface: fundamental investigations of tribology with atomic force microscopy,” *Chemical Reviews*, 97(4), pp. 1163-1194, 1997.

[14] P. Avouris, T. Hertel, and R. Martel, “Atomic force microscope tip-induced local oxidation of silicon: kinetics, mechanism, and nanofabrication,” *Applied Physics Letters*, 71(2), pp. 285-287, 1997.

[15] B. A. Gozen, and O. B. Ozdoganlar, “A rotating-tip-based mechanical nano-manufacturing process: nanomilling,” *Nanoscale Research Letters*, 5(9), pp. 1403-1407, 2005.

[16] B. Mokaberi, J. Yun, M. Wang, and A. A. Requicha, “Automated nanomanipulation with atomic force microscopes,” *IEEE International Conference on Robotics and Automation*, pp. 1406-1412, 2007.

[17] H. Xie, and S. Régnier, “High-efficiency automated nanomanipulation with parallel imaging/manipulation force microscopy,” *IEEE Transactions on Nanotechnology*, 11(1), pp. 21-33, 2012.

[18] A. Kaneta, R. Fujimoto, T. Hashimoto, K. Nishimura, M. Funato, and Y. Kawakami, “Instrumentation for dual-probe scanning near-field optical microscopy,” *Review of Scientific Instruments*, 83(8), pp. 083709, 2012.

[19] J. C. Acosta, J. Polesel-Maris, F. Thoyer, H. Xie, S. Haliyo and S. Régnier, “Gentle and fast atomic force microscopy with a piezoelectric scanning probe for nanorobotics applications,” *Nanotechnology*, 24(6), pp. 065502, 2013.

[20] E. Tsunemi, K. Kobayashi, K. Matsushige, and H. Yamada, “Development of dual-probe atomic force microscopy system using optical beam deflection sensors with obliquely incident laser beams,” *Review of Scientific Instruments*, 82(3), pp. 033708, 2011.

[21] E. Tsunemi, K. Kobayashi, N. Oyabu, M. Hirose, Y. Takenaka, K. Matsushige, and H. Yamada, “Development of multi-environment dual-probe atomic force microscopy system using optical beam deflection sensors with vertically incident laser beams,” *Review of Scientific Instruments*, 84(8), pp. 083701, 2013.

[22] H. Xie, and S. Régnier, "Development of a Flexible Robotic System for Multiscale Applications of Micro/Nanoscale Manipulation and Assembly," *IEEE Transactions on Mechatronics*, 16(2), pp. 266-276, 2011.

[23] J. L. Hutter, and J. Bechhoefer, "Calibration of atomic-force microscope tips," *Review of Scientific Instruments*, 64(7), pp.1868-1873, 1993.

[24] H. J. Butt, B. Cappella, and M. Kappl, "Force measurements with the atomic force microscope: Technique, interpretation and applications," *Surface Science Reports*, 59(1), pp.1-152, 2005.

[25] P. C. Hensen , V. pereyra, and G. Scherer, "The linear least squares problem," in *Least Squares Data Fitting with Applications* Baltimore: The Johns Hopkins University Press, 2013, pp. 25-33.

[26] L .L. Sohn, and R. L. Willett, "Fabrication of nanostructures using atomic-force-microscope-based lithography," *Applied Physics Letters*, 67(11), pp.1552-1554, 1995.

[27] B. Vasić, M. Kratzer, A. Matković, A. Nevosad, U. Ralević, D. Jovanović, C. Ganser, C. Teichert, and R. Gajić, "Atomic force microscopy based manipulation of graphene using dynamic plowing lithography," *Nanotechnology*, 24(1), pp.015303, 2012.

[28] R. W. Stark, G. Schitter, and A. Stemmer, "Tuning the interaction forces in tapping mode atomic force microscopy," *Physical Review B*, 68(8), pp. 85401, 2003.

[29] O. Smith, "Closer control of loops with dead time," *Chemical Engineering Progress*, 53(5), pp. 217-219, 1957.

[30] A. Bahill, "A simple adaptive smith-predictor for controlling time-delay systems: A tutorial," *IEEE Control systems magazine*, 3(2), pp.16-22, 1983.

SECTION

2. CONCLUSIONS

Though the atomic force microscope has the potential to be a powerful tool for nanoscale metrology, present challenges limit its use to very basic imaging and nanofabrication applications. This work addresses some of the prominent AFM challenges through novel feedback control methodologies. Current state-of-the-art AFM control designs involve thoroughly modeling the plant dynamics and incorporating it in the framework. However, the most important component, which is the dynamics induced by the sample is largely considered unknown and left out of the equation. The nature of the signals that arise from raster scanning a typical AFM sample was analyzed and categorized into two classes of quasiperiodic signals. A quasi-repetitive controller (QRC) was derived to asymptotically track the quasiperiodic signal classes. Experimental results demonstrate that QRC can provide greater than 3-fold increase imaging accuracy when compared to conventional PI controllers.

Another open challenge in AFM is that most of the nanofabrication processes are performed ‘blind’, i.e. in open-loop, due to the fundamental limitations of a single probe setup. In order to overcome this problem, a dual-probe AFM was designed and developed. Having two simultaneously operable probes provided the capability to monitor AFM processes in real-time. A feedback control design was developed to control plowing depth by imaging the plowing carried out by one probe using the other probe. Experimental results indicate plow depth can be controlled within ±1 nm accuracy. Such a framework can also be extended to control other tip-based AFM processes.

APPENDIX A.

LABVIEW PROGRAMS FOR DP-AFM OPERATION

LABVIEW PROGRAM

This appendix presents the details regarding the Labview program designed to operate the DP-AFM. The Labview program consists of three parts: (a) a real-time program that handles all the trajectory generation and motion control, (b) a FPGA program that processes both the PSD signals, and (c) a non real-time program running on the host which deals with image file handling and display. Figure A.1 shows the interconnections between different Labview programs. All programs are contained in the MAIN.lvproj file located in C:\ AFM_Master\MAIN folder.

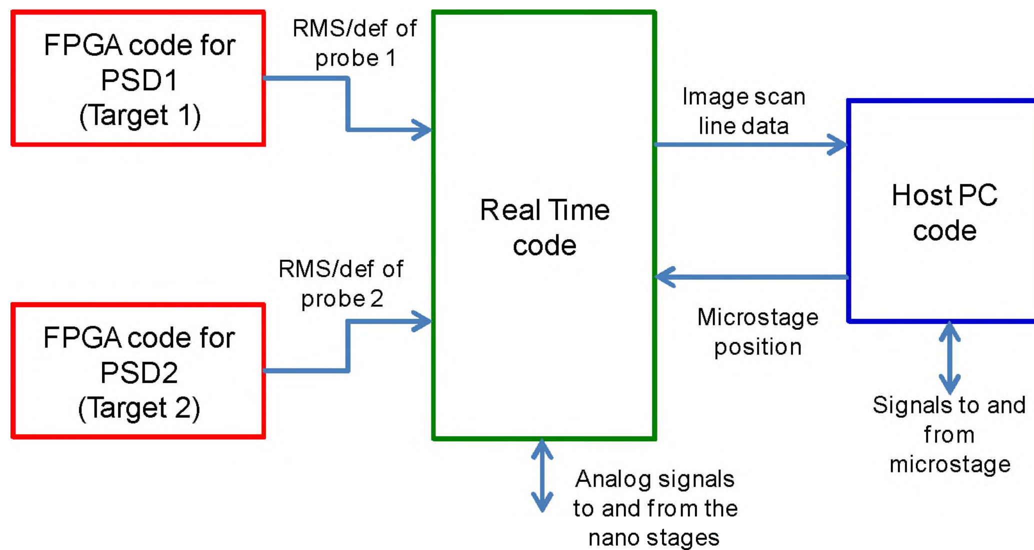

Figure A.1 Basic data flow representation between different Labview programs

(a) Labview FPGA program

Two identical FPGA programs with a basic structure as shown in Figure A.2 are compiled to run in FPGA targets 1 and 2. Each target is dedicated to a PSD. The NI

FlexRIO FPGA adapter modules (NI 5733 and NI 5734) installed on the FPFA targets sample signals at a fixed rate of 120 MHz. In order to carry out the filter calculations without the FPGA timing out the loop rate is reduced to 40 MHz and the PSD signals are down sampled. The signals are transferred from 120 MHz loop to 40 MHz loop using a direct memory access (DMA) FIFO for reliable data transmission. The signals are filtered using a 1st order low pass filter with a cut-off of 5 kHz. This filter acts as an anti-aliasing filter when the signals are transferred to the 10 kHz real-time loop. For purposes of tapping mode operation, the vertical PSD signal is further passed through a high pass filter to remove DC offset in the oscillating signal and then its RMS is calculated. The RMS signal is finally passes through an anti-aliasing filter and is read by the real-time loop.

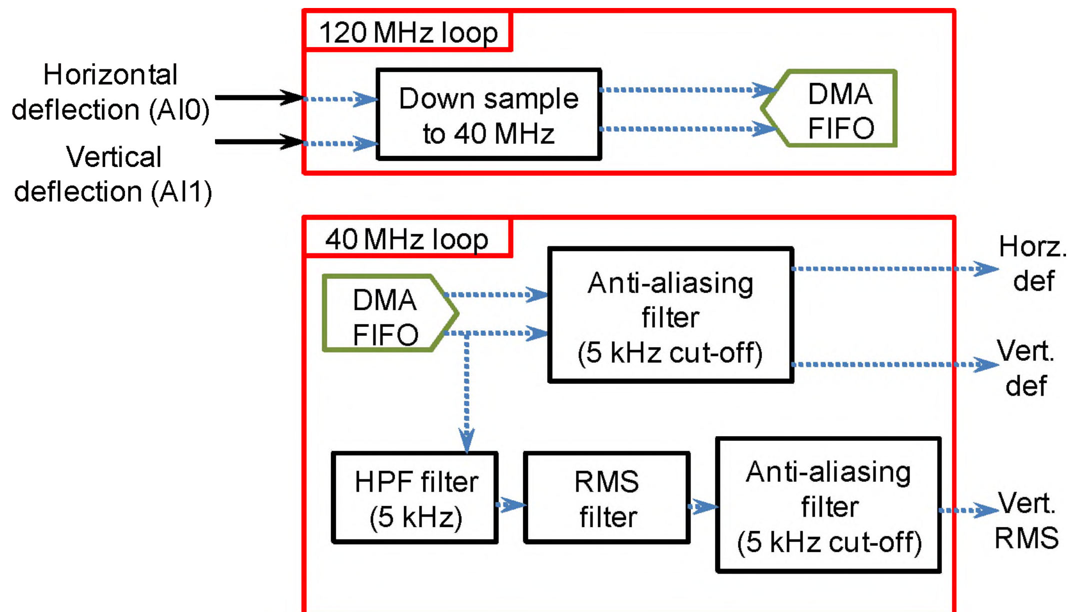

Figure A.2 Structure of the Labview FPGA program used to process the signals from the PSD

(b) Labview real-time program

The real-time program consist of three real-time loops and one non-real time while loop. The real-time loops run at 10 kHz and are synched by choosing a common clock (sample clock of AO card in slot 2 of the PXI target). General structure of the program is shown in Figure A.3. RT loop 1 is dedicated to reading the output from both the FPGA target. RT loop 2 is for trajectory generation and control of X & Y axes of all the stages (Hera XY, Pico 1 XY, Pico 2 XY). The XY axes control is in a separate loop to facilitate implementation of G-code in the future, when necessary. RT loop 3 is the main loop which deals with data acquisition and writing, Z axis control of all stages, scan line data generation. It consists of a state machine architecture that allows the program to smoothly jump between different AFM modes (disengage, engage, imaging, Haptic, plowing etc.). The non-real time while loop has operations that do not demand real-time implementation, including micro stage command module and dither piezo drive parameter setting. Inter loop data communication is handled by real-time FIFO variables with a buffer size of one. The real-time program communicates with the host PC through network shared variables. The 512 pixel line data and the micro stage commands are sent from the real-time program to the Labview program running in the host PC, and the current micro stage positions are sent back from the host program to the real-time program.

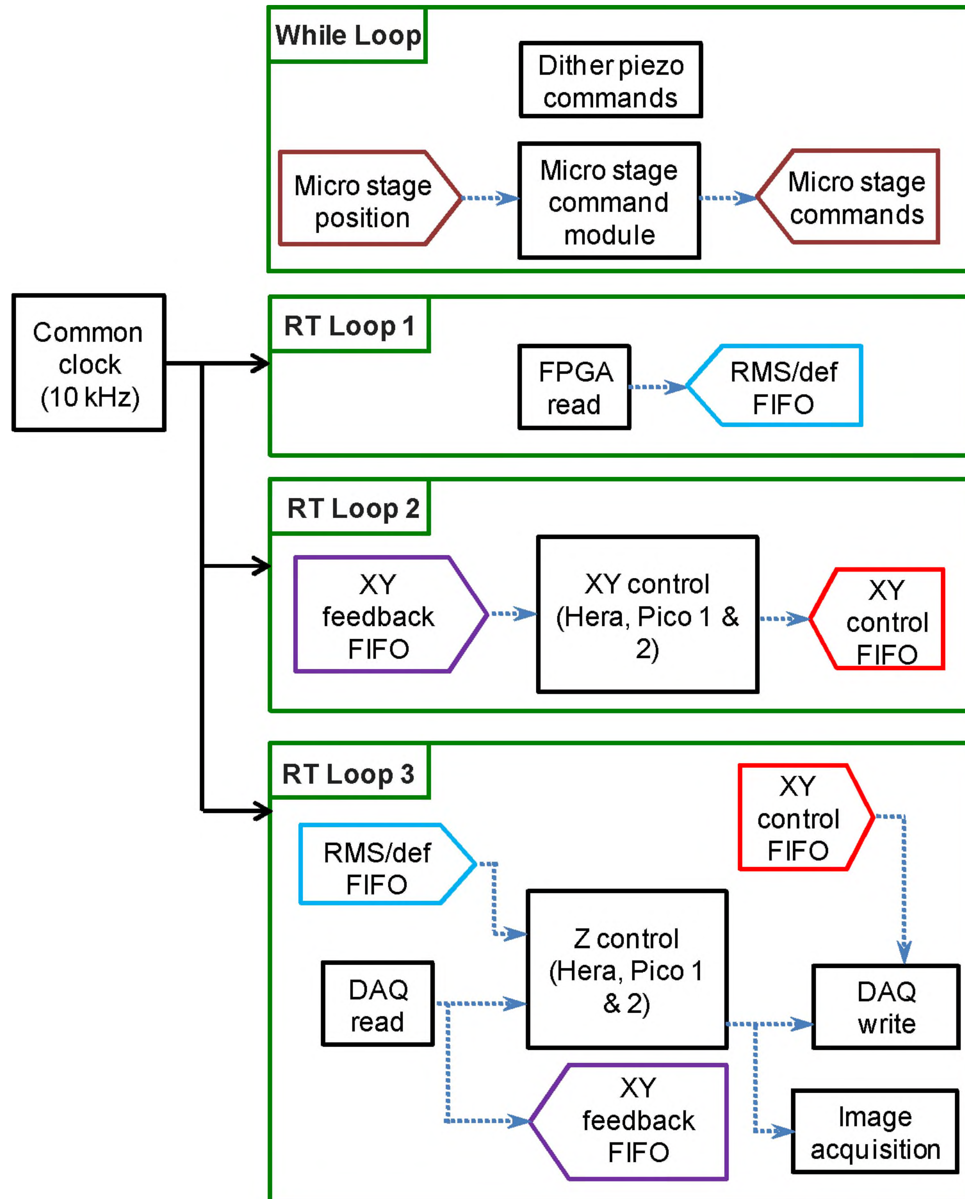

Figure A.3 Labview real-time program structure

(c) Labview host program

The Labview program running on the host PC consists of two independent while loops, each one dedicated to micro stage operation and image scan line data handling. The micro stage loop has the built-in VIs provided by PI to read and command all the

size micro stages. The other loop reads the individual image scan line data corresponding to both the probes and writes them in separate text files named im1_temp# and im2_temp#, where # is the line number. The files are stored in C:\Image_data\comm_data folder.

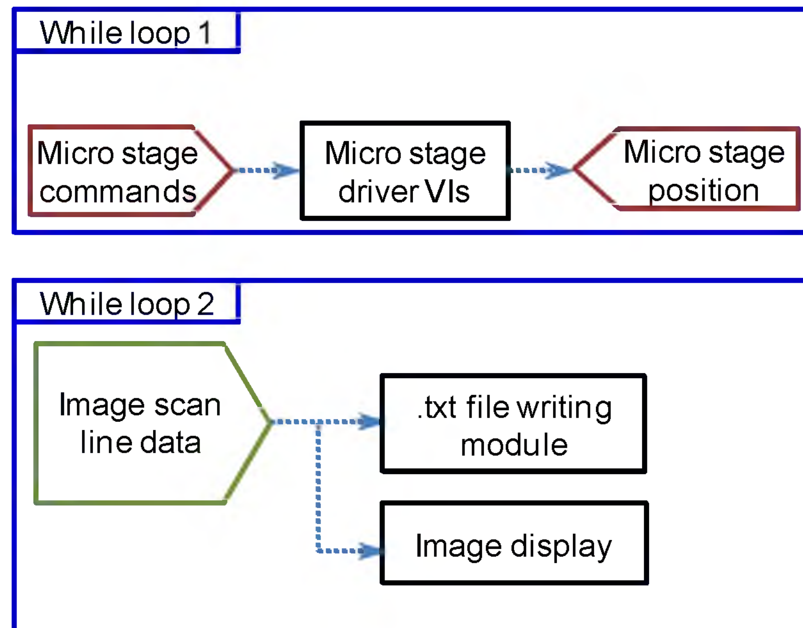

Figure A.4 Basic structure of the Labview host program

FRONT PANEL DESCRIPTIONS

I. Auto tune program – This program is an independent module used to find the resonant mode of a tapping cantilever. This is not part of the real-time program and should not be run simultaneously with any other ream-time program. This program runs at a lower loop rate of 200 Hz as the function generator card cannot vary frequencies at a faster rate. Figure A.5 shows the front panel of this program

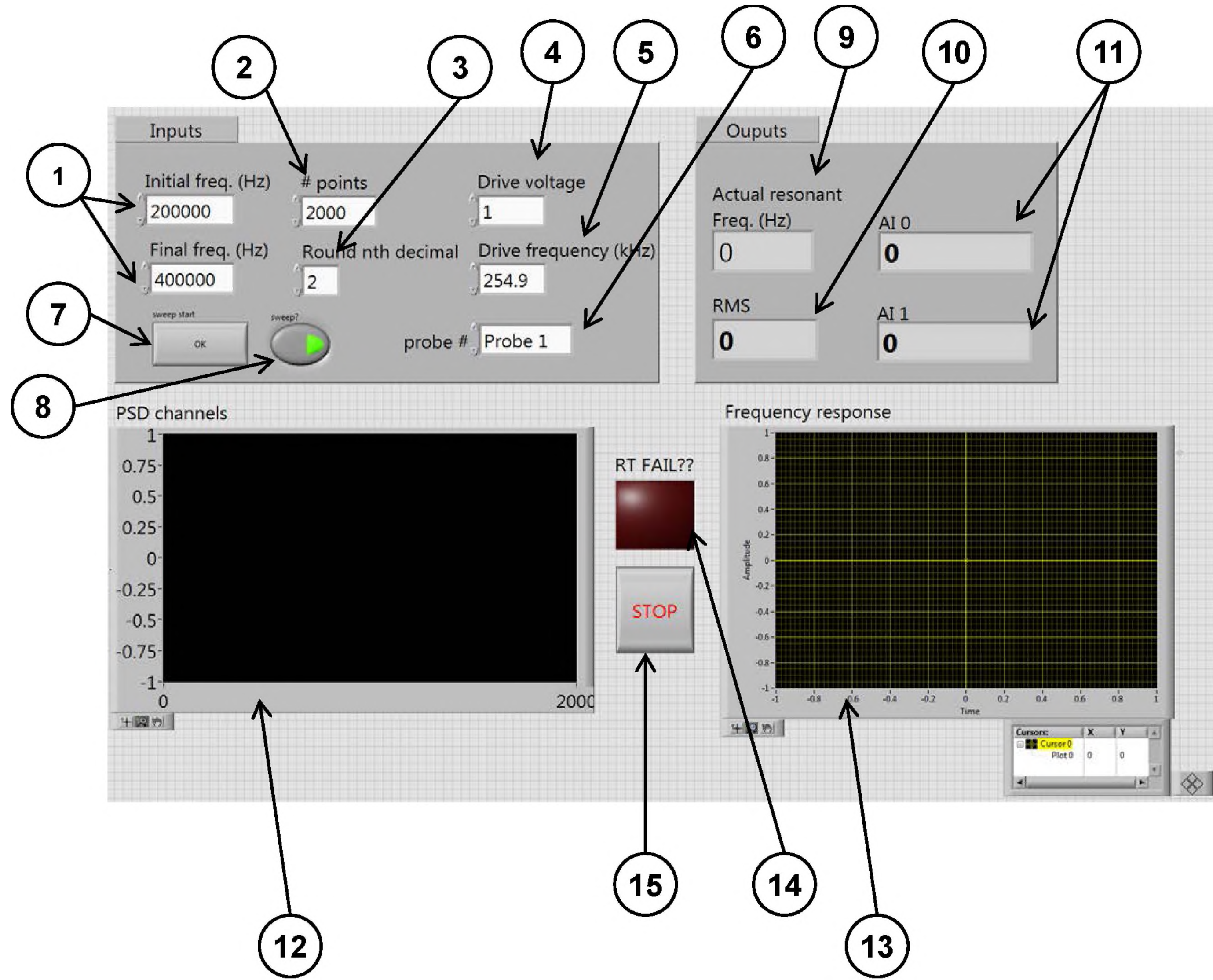

Figure A.5 Front panel of auto tune program

Description:

1. The frequency range to search for the resonant mode of the cantilever.
2. No. of data points required in the frequency sweep (frequency resolution)
3. No. of decimal places to round the frequency values
4. The drive voltage for the frequency sweep
5. The program will drive the cantilever at this frequency when 8 is switched off
6. Choose between probe 1 and 2 to perform the frequency sweep. It is recommended to restart the program when this option is changed.
7. Trigger to start the frequency sweep.
8. Sweep ON/OFF. This has to be ON to start the sweep using 7. When OFF the program will drive the cantilever at the frequency specifies in 5.
9. When the frequency sweep is completed the frequency of the resonant mode will be displayed here.
10. The FPGA RMS of the cantilever oscillation.
11. AI0 and AI1 (horizontal and vertical deflection) channel output.
12. Chart display of AI0 and AI1 values.
13. Frequency sweep display
14. LED switches on if the RT program fails.
15. STOP button to stop the program

II. Real-time program -

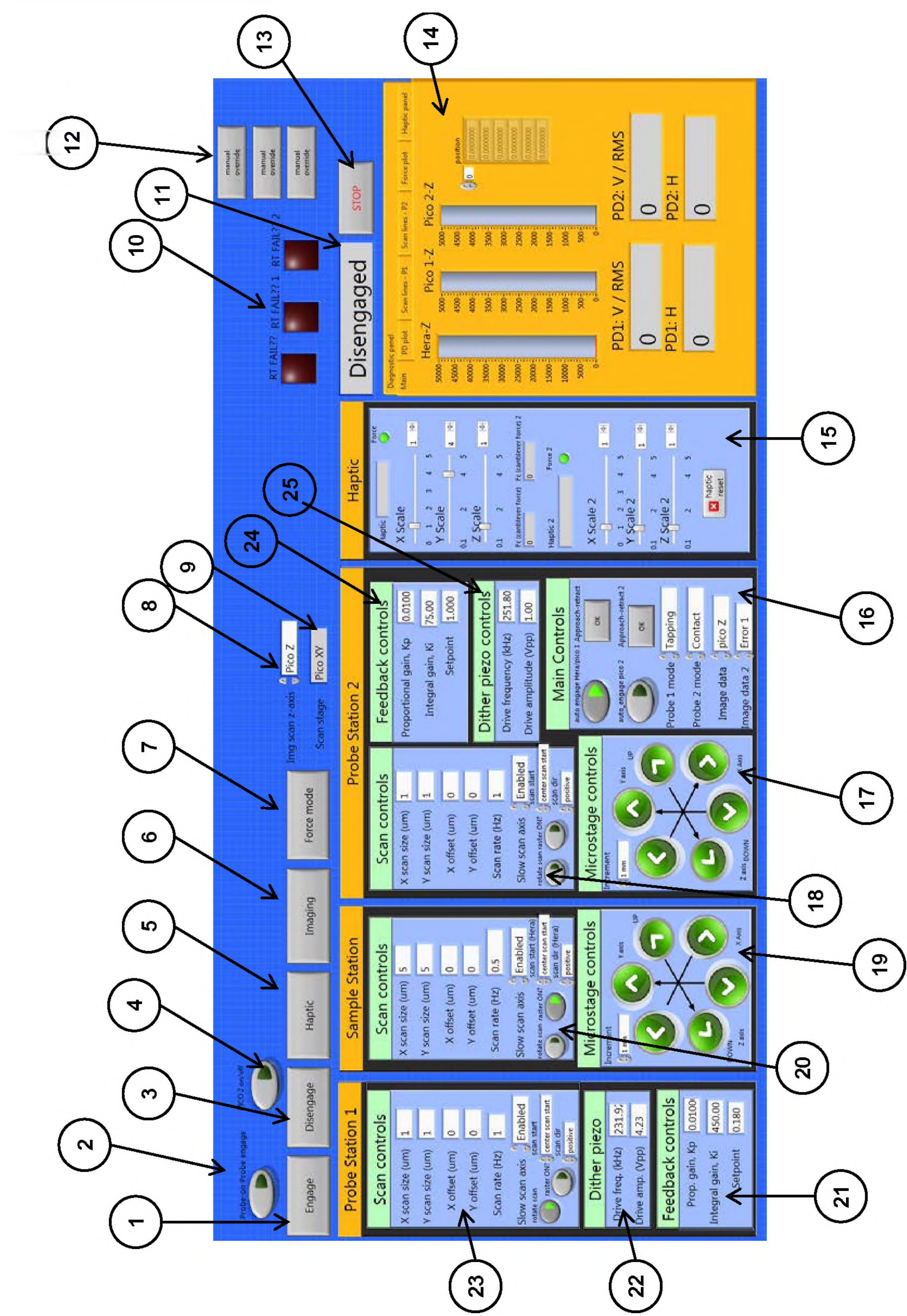

Figure A.6 Front panel of the main real-time program

Description:

1. The program has different modes – (a) disengaged, (b) engaging, (c) imaging, (d) Haptic, (e) plowing. By default the program starts in disengaged mode. Engage button initiates the auto engage module to bring the probe closer to the sample with a step size of 100 nm.
2. Enables searching one probe with the other probe in 2D.
3. Disengage button moves the probe away from the sample by 2 µm when pressed in any mode. It is strongly recommended to disengage the probe before stopping the program.
4. Switches off the relevant sub VIs related to Pico cube 2. When operating only the first probe Pico cube 2 can be switched off with this button.
5. Pressing this button when imaging switches the program to haptic mode. Note: works **only** when the probe is in imaging mode.
6. Pressing this button while in haptic mode switches the program back to imaging mode.
7. Pressing this button when imaging switches the program to force mode. Note: works **only** when the probe is in imaging mode.
8. Choose which z axis (pico1 Z or Hera Z) should be used to imaging when operating a single. **Switch this to Pico Z during dual-probe operation.**
9. Choose the XY stage that should be used for raster scanning. During dual-probe operation this can be set to Hera XY to get perform synchronized scanning.
10. LEDs turn ON if any one of the iteration of any real-time loops fails.
11. Status of the program indicating which mode is currently active

12. Separate manual override switches to switch OFF the LEDs (10). If the LEDs turn ON rarely they can be reset using these switches. If they turn ON frequently then the program needs to be stopped.
13. Stop button stops the program altogether. Note: make sure the program is in disengaged mode before stopping the program.
14. Control panel which has multiple mode-based options. Choose the relevant tab to access these options.
15. Haptic control panel. Active only when the program is in haptic mode.
16. Main control panel. It includes option to choose between contact and tapping mode for both the probes, switch ON/OFF auto engage of each probe. The approach-retract buttons enable one iteration of the approach-retract routine.
17. Micro stage controls for probe 2 micro stage. Note: This panel is active during all the program modes. Care should be taken not to press these buttons accidently during any of the AFM operation. Same applies to 19.
18. Scan control for pico cube 2. Disabling the slow scan axis makes the probe scan the same spot repeatedly. Scan start menu provides an option to start the scan at the center or at the edge of the scan range. Scan dir. option changes the direction of the slow scan axis.
19. Micro stage controls for sample micro stage.
20. Scan controls for Hera XY.
21. Feedback controls for probe 1. The set point and gain values have to be changed depending on the AFM mode (contact or tapping),

22. The drive voltage and frequency of the probe 1 dither piezo. Available only in tapping mode (when probe 1 mode is set to tapping in 16)
23. Scan control for Pico cube 1.
24. Feedback controls for probe 2.
25. Dither piezo drive voltage and frequency of the probe 2 dither piezo.

III. Plowing module – Plowing module can be used to plow samples along the longitudinal axis of the cantilever. Plowing can only be done with probe 1. In closed loop plowing probe 1 is assumed to be the plowing probe and probe 2 as the imaging probe. Figure A. 7 shows the plowing module options.

Description:

1. Tabs in the panel can be used to access options based on the program mode. Choose plowing to access the options shown in Figure A.6.
2. The nominal plowing process gain, $\bar{K}$.
3. Reference plow depth in nm.
4. To plow, this button has to be ON before the program reaches the 'engaging' mode. If this button is ON then the program directly goes into plowing mode once the probe engages. If it is OFF then the program goes to imaging mode from engaging mode.
5. Chart display used to plot the process variables.

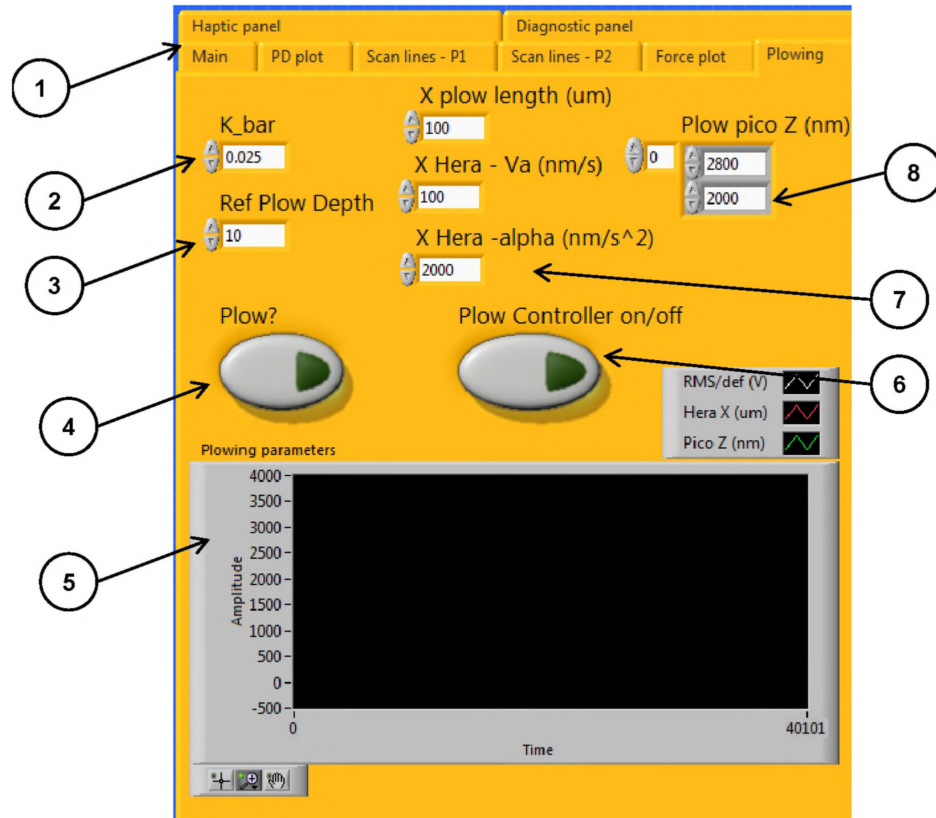

Figure A.7 Front panel of the plowing module

6. Switching ON this button activates the closed loop plowing process. For open loop plowing this button should be switched OFF.
7. Options used to set the plow length, magnitude of the velocity and acceleration along the X direction, which is the plow direction. Note that the velocity and acceleration are magnitudes. To change the plow direction provide a negative value for ‘X plow length’ option, but maintain positive velocity and acceleration values.

8. The commanded Pico 1 Z displacement while plowing in open-loop. The first element is the initial position and the second element is final position.

IV. Host PC program -

Description:

1. Clears the image arrays holding the pixel information .This also clears the plots 5 and 6.
2. Emergency button which lowers the Z axis of the sample micro stage. Use it when the communication between the real-time and the host program fails during AFM operation.
3. Button used to activate the changes made in 7 and 8.
4. 2D plot of the data being sent from real time. Typically image generated by probe 1 is displayed here.
5. 2D plot of the data being sent from real time. Typically image generated by probe 2 is displayed here.
6. Image display controls corresponding to 6.It can be used to set X and Y axes scale, rotate the image update direction, and flip the axes. It can also be used to switch the display between raw and flattened images.
7. Same as 7 but for the 2D plot in 5.
8. Row numbers and file numbers corresponding to each image date.
9. STOP button stops the entire program

10. Controls used to vary the images size from conventional 512x512 pixel size to custom values. Note: In order for this to work the real-time data should send the same amount of pixel data.
11. Current position of the all micro stages.
12. The file path where the image scan line data has to be stored. Each scan line data is stored as 512 size vector. Data displayed in 5 and 6 are stored with the file names Im1_temp# and Im2_temp#, where # is the file number generated by the program.

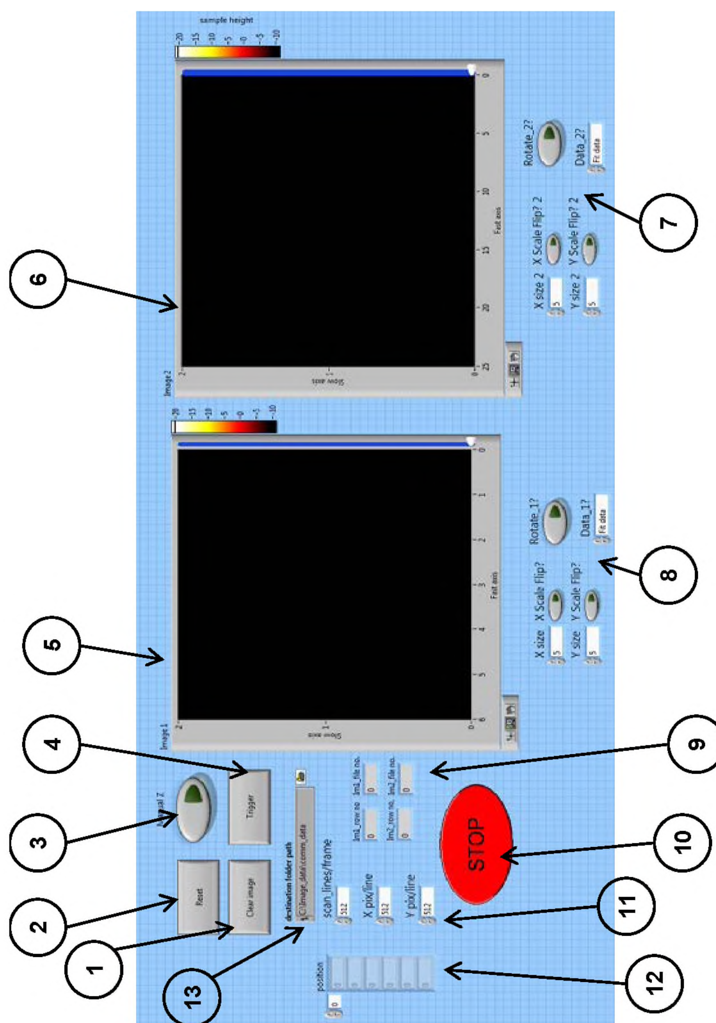

Figure A.8 Front panel of the host PC program

APPENDIX B.

MATLAB PROGRAMS FOR AFM IMAGE PROCESSING

Program to read image files written by Labview

The program provided below reads the individual scan data from C:\Image_data\comm_data folder and provides 512x512 matrix for further post processing.

CODE:

```
clc;
clear all;
close all;
flag=2;
i=1;
imagearray=ones(512); % Scan lien data size (default = 512)
imagearray_1=zeros(512);
% Enter the folder path where temp data is stored
folder_path='C:\Image_data\comm_data\';
maxT=2;
minT=-2;
% Loop runs until file does not exist (flag!=2)
while flag==2
    I=num2str(i);
    path=strcat(folder_path,'Im1_temp',I);
    % change file name to Im2_temp to read probe 2 data
    flag=exist(path,'file');
    if flag==2
    mag=load(path);
    count(i)=mag(1);
    imagearray(count(i),:)= mag(2:end);
colormap copper
imagesc(imagearray);
caxis([-10 10]);
    drawnow;
    end
    i=i+1;
end
```

Least square line fit to flatten AFM images

Program fits a best line, in least square sense, to individual scan lines and subtracts it from the raw data to provide a flattened version of the original image.

CODE:

```
%% LINE FIT
clc;
close all;
RAW=imagearray;                          % raw image data
n=size(RAW);
im_line_fit=zeros(n);
xs=n(1);ys=n(2);
fitt=zeros(ys,1);

for i=1:xs
    P=polyfit(1:ys,RAW(i,:),1);      % Linear polynomial fit to row data
    fitt=polyval(P,1:ys);
    im_line_fit(i,:)=RAW(i,:)-fitt;
end
surf(RAW,'edgecolor','none')
Figure
surf(im_line_fit,'edgecolor','none')
```

Lease square plane fit to flatten AFM images

Same as the previous program except the program fits a plane to the entire image data and subtracts it to provide better flattening effect compared to line fit. The least square plane fit solution for a 2D matrix with *m* elements, and coordinates (*x,y,z*), is of the form $z = Ax + By + C$, where

$$\begin{bmatrix} A \\ B \end{bmatrix} = \begin{bmatrix} \sum_{i=1}^{m}(x_i - \bar{x})^2 & \sum_{i=1}^{m}(x_i - \bar{x})(y_i - \bar{y}) \\ \sum_{i=1}^{m}(x_i - \bar{x})(y_i - \bar{y}) & \sum_{i=1}^{m}(y_i - \bar{y})^2 \end{bmatrix}^{-1} \begin{bmatrix} \sum_{i=1}^{m}(x_i - \bar{x})(z_i - \bar{z}) \\ \sum_{i=1}^{m}(z_i - \bar{z})(y_i - \bar{y}) \end{bmatrix}$$

$$C = \bar{z} - A\bar{x} - B\bar{y}$$

$$\bar{x} = \frac{1}{m}\sum_{i=1}^{m} x_i; \quad \bar{y} = \frac{1}{m}\sum_{i=1}^{m} y_i; \quad \bar{z} = \frac{1}{m}\sum_{i=1}^{m} z_i;$$

CODE:

```
%% PLANE FIT
clc;
close all
RAW=imagearray;
```

```
n=size(RAW);
fitt=zeros(n);
xs=n(1);ys=n(2);
x=(1:xs)';
y=(1:ys)';
L=xs*ys;
X=zeros(L,1);Y=zeros(L,1);Z=zeros(L,1);
c=0;
% transforming X, Y, Z date into 1D arrays
for i=1:xs
    for j=1:ys
        c=c+1;
        X(c)=x(i);
        Y(c)=y(j);
        Z(c)=RAW(i,j);
    end
end
% Computing the individual mean
C=mean(Z);
mm=[mean(X) mean(Y)]';
X=X-mean(X);Y=Y-mean(Y);Z=Z-mean(Z);
Xsq=sum(X.*X);
Ysq=sum(Y.*Y);
XY=sum(X.*Y);
XZ=sum(X.*Z);
YZ=sum(Y.*Z);
M=[Xsq XY;XY Ysq];

S= [M\[XZ YZ]'];
ss=C-S(1:2)'*mm;
S=[S;ss];
for i=1:xs
    for j=1:ys
        fitt(i,j)=S'*[i j 1]';
    end
end
im_fit=RAW-(fitt);
```

BIBLIOGRAPHY

[1] G. Binnig and C. F. Quate, “Atomic Force Microscope,” *Physical Review Letters*, 56(9), pp. 930-933, 1986.

[2] S. Alexander, L. Hellemans, O. Marti, J. Schneir, V. Elings, P. K. Hansma, M. Longmire and J. Gurley, “An atomic-resolution atomic-force microscope implemented using an optical lever,” *Journal of Applied Physics*, *65*(1), pp.164-167, 1989.

[3] I. Tanaka, I. Kamiya, H. Sakaki, N. Qureshi, S. J. Allen Jr and P. M. Petroff, “Imaging and probing electronic properties of self-assembled InAs quantum dots by atomic force microscopy with conductive tip,” *Applied physics letters*, *74*(6), pp.844-846, 1999.

[4] R. Garcia and R. Perez, “Dynamic atomic force microscopy methods,” *Surface Science Reports*, 47, pp. 197-301, 2002.

[5] N. Jalili and K. Laxminarayana, “A review of atomic force microscopy imaging systems: application to molecular metrology and biological sciences,” *Mechatronics*, 14, pp. 907-945, 2004.

[6] S. I. Kitamura, and M. Iwatsuki, “High-resolution imaging of contact potential difference with ultrahigh vacuum noncontact atomic force microscope,” *Applied Physics Letters*, 72(24), pp. 3154-3156, 1998.

[7] A. L. Weisenhorn, P. K. Hansma, T. R. Albrecht and C. F. Quate, “Forces in atomic force microscopy in air and water,” *Applied Physics Letters*, *54*(26), pp.2651-2653, 1989.

[8] C. A. Putman, K. O. Van der Werf, B. G. De Grooth, N. F. Van Hulst, and J. Greve, “Tapping mode atomic force microscopy in liquid,” *Applied Physics Letters*, *64*(18), pp. 2454-2456, 1994.

[9] T. Nitta, H. Haga, K. Kawabata, K. Abe, and T. Sambongi, “Comparing microscopic with macroscopic elastic properties of polymer gel,” *Ultramicroscopy*, *82*(1), pp. 223-226, 2000.

[10] J. J. Saenz, N. Garcia, P. Grütter, E. Meyer, H. Heinzelmann, R. Wiesendanger, L. Rosenthaler, H. R. Hidber, and H. J. Güntherodt, “Observation of magnetic forces by the atomic force microscope,” *Journal of Applied Physics*, *62*(10), pp. 4293-4295, 1987.

[11] S. J. T. Van Noort, O. H. Willemsen, K. O. van der Werf, B. G. de Grooth, and J. Greve, “Mapping electrostatic forces using higher harmonics tapping mode atomic force microscopy in liquid,” *Langmuir*, *15*(21), pp. 7101-7107, 1999.

[12] T. R. Rodrıguez and R. García, "Compositional mapping of surfaces in atomic force microscopy by excitation of the second normal mode of the microcantilever," *Applied Physics Letters*, *84*(3), pp.449-451, 2004.

[13] R. Garcia, and A. San Paulo, "Attractive and repulsive tip-sample interaction regimes in tapping-mode atomic force microscopy," *Physical Review B*, *60*(7), p.4961, 1999.

[14] M. L. Bloo, H. Haitjema and W. O. Pril, "Deformation and wear of pyramidal, silicon-nitride AFM tips scanning micrometre-size features in contact mode," *Measurement*, *25*(3), pp.203-211, 1999.

[15] B. Mokaberi and A. A. Requicha, "Drift compensation for automatic nanomanipulation with scanning probe microscopes," *IEEE Transactions on Automation Science and Engineering*, *3*(3), pp.199-207, 2006.

[16] S.M. Hues, C. F. Draper, K. P. Lee and R. J. Colton, "Effect of PZT and PMN actuator hysteresis and creep on nanoindentation measurements using force microscopy," *Review of scientific instruments*, *65*(5), pp.1561-1565, 1994.

[17] D. Croft, G. Shedd and S. Devasia, "Creep, hysteresis, and vibration compensation for piezoactuators: atomic force microscopy application," In *Procedings of the American Control Conference,* Vol. 3, pp. 2123-2128, 2000.

[18] M. Loganathan, S. R. Kodandarama and D. A. Bristow, "Measurement sensitivity improvement in tapping-mode atomic force microscopy through bi-harmonic drive signal," *Review of Scientific Instruments*, *82*(10), pp.103704, 2011.

[19] A. Sebastian, A. Gannepalli and M. V. Salapaka, "A review of the systems approach to the analysis of dynamic-mode atomic force microscopy," *IEEE Transactions on Control Systems Technology*, *15*(5), pp.952-959, 2007.

[20] T. R. Albrecht, P. Grütter, D. Horne and D. Rugar, "Frequency modulation detection using high-Q cantilevers for enhanced force microscope sensitivity," *Journal of Applied Physics*, *69*(2), pp.668-673, 1991.

[21] T. Fukuma, J. I. Kilpatrick and S. P. Jarvis, "Phase modulation atomic force microscope with true atomic resolution," *Review of scientific instruments*, *77*(12), p.123703, 2006.

[22] K. K. Leang, Q. Zou and S. Devasia, "Feedforward control of piezoactuators in atomic force microscope systems," *IEEE Control Systems*, *29*(1), pp.70-82, 2009.

[23] Y. Wang, J. Wan, X. Hu, L. Xu, S. Wu and X. Hu, "A rate adaptive control method for Improving the imaging speed of atomic force microscopy," *Ultramicroscopy*, *155*, pp.49-54, 2015.

[24] A. Sebastian, M. V. Salapaka and J. P. Cleveland, “Robust control approach to atomic force microscopy,” In 42nd IEEE Conference *Decision and Control,* Vol. 4, p. 3443-3444, 2003.

[25] A. Noy, C. D. Frisbie, L. F. Rozsnyai, M. S. Wrighton and C. M. Lieber, “Chemical force microscopy: exploiting chemically-modified tips to quantify adhesion, friction, and functional group distributions in molecular assemblies,” *Journal of the American Chemical Society*, *117*(30), pp.7943-7951, 1995.

[26] W. M. D. Wright and D. G. Chetwynd, “Can charge writing aid nanotechnological manipulation?” *Nanotechnology*, *9*(2), p.133, 1988.

[27] R. D. Piner, J. Zhu, F. Xu, S. Hong and C. A. Mirkin, “Dip-pen nanolithography,” *science*, *283*(5402), pp.661-663, 1999.

[28] S. W. Lee, R. G. Sanedrin, B. K. Oh and C. A. Mirkin, “Nanostructured Polyelectrolyte Multilayer Organic Thin Films Generated via Parallel Dip-Pen Nanolithography,” *Advanced Materials*, *17*(22), pp.2749-2753, 2005.

[29] Y. Li, W. Maynor, J. Liu, “Electrochemical AFM Dip-Pen Nanolithography,” *Journal- American Chemical Society*, *123*(9), pp. 2105-2106, 2001.

[30] J. H. Lim and C. A. Mikin, “Electrostatically Driven Dip-Pen Nanolithography of Conducting Polymers,” *Advanced Materials*, *14*(20), pp. 1474–1477, 2002.

[31] K. Lee, J. Lim, C. A. Mirkin, “Protein Nanostructures formed via Direct-Write Dip-Pen Nanolithography,” *Journal- American Chemical Society*, *125*(19), pp. 5588-5589, 2003.

[32] E. Tsunemi, K. Kobayashi, K. Matsushige and H. Yamada, "Development of dual-probe atomic force microscopy system using optical beam deflection sensors with obliquely incident laser beams,” *Review of Scientific Instruments*, *82*(3), p.033708, 2011.

[33] E. Tsunemi, K. Kobayashi, N. Oyabu, M. Hirose, Y. Takenaka, K. Matsushige and H. Yamada, “Development of multi-environment dual-probe atomic force microscopy system using optical beam deflection sensors with vertically incident laser beams,” *Review of Scientific Instruments*, *84*(8), p.083701, 2013.

[34] T. Nakayama, O. Kubo, Y. Shingaya, S. Higuchi, T. Hasegawa, C. S. Jiang, T. Okuda, Y. Kuwahara, K. Takami and M. Aono, “Development and Application of Multiple-Probe Scanning Probe Microscopes,” *Advanced materials*, *24*(13), pp.1675-1692, 2012.

[35] J. C. Acosta, J. Polesel-Maris, F. Thoyer, H. Xie, S. Haliyo and S. Régnier, "Gentle and fast atomic force microscopy with a piezoelectric scanning probe for nanorobotics applications," *Nanotechnology*, *24*(6), p.065502, 2013.

[36] A. Bolopion, H. Xie, D. S. Haliyo and S. Régnier, "Haptic teleoperation for 3-d microassembly of spherical objects," *IEEE/ASME Transactions on Mechatronics*, *17*(1), pp.116-127, 2012.

[37] M. Tomizuka, T. C. Tsao, and K. K. Chew, "Discrete-time domain analysis and synthesis of repetitive controllers," *Proceedings of the 1988 American Control Conference*, pp. 860-866, 1988.

[38] S. Hara, Y. Yamamoto, T. Omata and M. Nakano, "Repetitive control system: a new type servo system for periodic exogenous signals," *IEEE Transcations on Automatic Control*, *33*, pp. 659-668, 1988.

[39] B. A. Francis and W. M. Wonham, "The internal model principle for linear multivariable regulators," *Applied Mathematics and Optics*, *2*, pp. 170-194, 1975.

[40] K. K. Chew and M. Tomizuka, "Digital control of repetitive errors in disk drive systems," *Proceedings of the American Control Conference*, pp. 540-548, 1990.

[41] J. Moon, M. Lee and M. Chung, "Repetitive control for the track-following servo system of an optical disk drive," *IEEE Transactions on Control systems Technology*, *6*(*5*), pp. 663-670, 1998.

[42] Y.Y. Tzou, R. S. Ou, S. L. Jung, and M. Y. Chang, "High-performance programmable AC power source with low harmonic distortion using DSP-based repetitive control technique." *IEEE Transactions on Power Electronics*, *12*(4), pp.715-725, 1997.

[43] G. Hilllerstrom, "Adaptive suppression of vibrations- a repetitive control approach," *IEEE Transactions on Control Systems Technology*, *4*(1), pp. 72-77, 1996.

[44] S. Daley, J. Hatonen, and D. H. Owens, "Active vibration isolation in a "small spring" mount using a repetitive control approach," *Control Engineering Practice*, *14*(9), pp. 991-997, 2006.

[45] C. L. Chen and G. C. Chiu, "Compensating for spatially repetitive disturbance with linear parameter varying repetitive control," *Proceedings of the 2004 IEEE International Conference on Control Applications,* Vol. 1, pp. 736-741, 2004.

[46] E. Kurniawan, Z. Cao, and Z. Man, "Design of robust repetitive control with time-varying sampling periods," *IEEE Transactions on Industrial Electronics, 61*(6), 2014, pp. 2834-2841.

[47] Z. Cao and G. F. Ledwich. "Adaptive repetitive control to track variable periodic signals with fixed sampling rate," *IEEE Transactions on Mechatronics*, *7*(3), pp. 378-384, 2002.

[48] H. G. Dotsch, H. T. Smakman, P. M Van den Hof and M. Steinbuch, " Adaptive repetitive control of a compact disc mechanism," *Proceedings of the 34th IEEE Conference on Decision and Control* , Vol. 2, pp. 1720-1725, 1995.

VITA

Muthukumaran Loganathan was born in Tamil Nadu, India. He obtained his bachelor degree in Mechanical Engineering in May 2010 from Anna University, India. He joined Missouri University of Science and Technology in fall 2010 to pursue Masters in Mechanical Engineering and graduated in fall 2012. In spring 2013, he started his Ph.D. in Mechanical Engineering. He worked in the Precision Motion Control lab (PMCL) under Dr. Douglas Bristow. In July 2017, he received his Ph.D. in Mechanical Engineering from Missouri University of Science & Technology.